**Title:**

# Reduced Thalamic Excitation to Motor Cortical Pyramidal Tract Neurons in Parkinsonism

Liqiang Chen[1], Samuel Daniels[1], Rachel Dvorak[1], and Hong-Yuan Chu[1,*]

[1]Department of Neurodegenerative Science, Van Andel Research Institute, Grand Rapids, MI 49503 USA

[*]Correspondence: hongyuan.chu@vai.org

Address: 333 Bostwick Ave NE, Grand Rapids, MI 49503

Phone: 616-234-5847

**Author contribution**: Investigation, formal analysis: L.C., S.D., R.D., and H.Y.C.; Conceptualization, funding acquisition, project administration, resources, supervision, visualization, writing – original draft: H.Y.C.; Writing – review& editing: L.C., S.D., and H.Y.C.

**Competing interests**: The authors declare no competing interests.

**Acknowledgement**: The authors thank the Van Andel Research Institute optical imaging core for the advanced confocal microscope, and Van Andel Research Institute vivarium for animal husbandry. The authors thank all members of the Chu lab at Van Andel

Research Institute for thoughtful discussions. Funding: This work was supported by the National Institute of Neurological Disorders and Stroke (grant#: R01NS121371).

**Abstract**

Degeneration of midbrain dopaminergic (DA) neurons alters the connectivity and functionality of the basal ganglia-thalamocortical circuits in Parkinson's disease (PD). Particularly, the aberrant outputs of the primary motor cortex (M1) contribute to parkinsonian motor deficits. However, cortical adaptations at cellular and synaptic levels in parkinsonian state remain poorly understood. Using multidisciplinary approaches, we found that DA degeneration induces cell-subtype- and input-specific reduction of thalamic excitation to M1 pyramidal tract (PT) neurons. At molecular level, we identified that NMDA receptors play a key role in mediating the reduced thalamocortical excitation to PT neurons. At circuit level, we showed that the decreased thalamocortical transmission in parkinsonian mice can be rescued by chemogenetically suppressing basal ganglia outputs. Together, our data suggest that cellular and synaptic adaptions in M1 neuron subtypes contribute to the reduced cortical outputs in parkinsonian state and are important aspects of PD pathophysiology.

**Teaser**

Specific motor cortical plasticity contributes to Parkinson's pathophysiology in mouse models of the disease.

**Key words**

Dopamine, motor cortex, thalamus, basal ganglia, Parkinson's disease, 6-hydroxydopamine, optogenetics, chemogenetics, electrophysiology, NMDA receptor

## Introduction

Degeneration of dopaminergic (DA) neurons in the substantia nigra pars compacta (SNc) alters the magnitude and temporal pattern of basal ganglia (BG) outputs to downstream motor regions and is causally linked with the motor deficits in Parkinson's disease (PD) (*1–3*). The substantia nigra pars reticulata (SNr) is the major BG output structure in rodents and sends GABAergic projections to the inhibitory BG-recipient territory of the motor thalamus (BGMT), including the ventral anterior-lateral (VAL) and ventromedial (VM) thalamus (*4–8*). The motor thalamus transmits motor selection and execution information to cortical regions for proper motor control (*6*, *9–11*). Thus, the thalamocortical network occupies a critical position in mediating motor symptoms of PD, particularly those related to skilled motor activities (*12–16*).

The primary motor cortex (M1) plays a key role in sensorimotor integration and proper control of motor behaviors (*17–19*). Its involvement into pathophysiology of parkinsonian motor deficits was proposed by the rate model of BG-thalamocortical network and further supported by recent experimental evidence (*1*, *12–14*, *20–22*). It is noteworthy to note that M1 is a laminar structure that comprises distinct subtypes neurons and receives long-range cortical and subcortical inputs. How do basal ganglia dysfunction and/or loss of DA neuromodulation affect the connectivity and function of M1 network in PD? How does M1 circuit dysfunction at systematic and cellular levels contribute to PD symptoms? Answers to these questions will advance our understanding of PD pathophysiology at circuit level.

A growing amount of evidence suggests that M1 circuits exhibit specific alterations in parkinsonism. Loss of SNc DA neurons alters neuronal firing and synaptic connectivity

of M1 pyramidal neurons (*12*, *23*–*25*). Particularly, DA depletion selectively affects the activity of pyramidal tract (PT) neurons, but not the intratalencephalic (IT) neurons, in the layer (L) 5 of M1 (*12*, *14*, *21*, *22*, *26*, *27*). These structural and functional changes perhaps contribute to the rewired cortical motor representation and impaired forelimb function in parkinsonian state (*28*–*30*). Building on these observations, we further studied the changes of glutamatergic synapses arising from the BGMT to M1 pyramidal neuron subtypes in parkinsonian mice. We therefore hypothesized that degeneration of SNc DA neurons induces cell-subtype- and input-specific adaptations at thalamocortical synapses and that the synaptic adaptations are driven by basal ganglia dysfunction. Our results largely agreed with our predictions and provided detailed description and mechanistic understanding of thalamocortical synaptic adaptations in parkinsonian state.

## Results

Mice received either 6-OHDA injection into the medial forebrain bundle (MFB) to induce the degeneration of nigrostriatal pathway and SNc DA neurons ("6-OHDA mice" hereafter), or vehicle injection into the MFB as controls ("controls" hereafter). Physiological and anatomical studies were conducted between 3–5 weeks post-injections. To confirm a complete degeneration of nigrostriatal DA pathway in 6-OHDA mice, animals were subject to behavioral tests at 3 weeks post-surgery, prior to electrophysiology and anatomy experiments (*26*). Relative to controls, 6-OHDA mice showed a significantly reduced locomotor activity in an open field arena (distance travelled in 10 min, control = 39 [33–48] m, n = 51 mice; 6-OHDA = 21 [15–27] m, n = 52 mice; $p < 0.0001$, MWU test). Moreover, 6-OHDA mice also exhibited asymmetric forelimb use in cylinder test (% of ipsilateral forelimb use, controls = 50 [49–52]%, n = 51 mice; 6-OHDA = 85 [79–93]%, n = 52 mice; $p < 0.0001$, MWU test). *Post hoc* immunostaining of striatal TH was conducted, which showed a > 80% loss of striatal TH immunoreactivity (TH-ir) in the lesioned hemisphere of 6-OHDA mice ($\%TH_{ipsilateral/contralateral\ striatum}$, control = 100 [97–102]%, n = 51 mice; 6-OHDA = 11 [7–16]%, n = 52 mice; $p < 0.0001$, MWU test). In a subset of animals, we assessed the TH-ir from M1, but found no significant change from either control or 6-OHDA mice ($\%TH_{ipsilateral\ M1/contralateral\ M1}$, control = 93 [85–103]%, n = 16 mice; 6-OHDA = 96 [89–109]%, n = 15 mice; $p = 0.52$, MWU test), indicating that 6-OHDA injection into the MFB did not affect the mesocortical pathway arising from the ventral tegmental area to M1 in the present study.

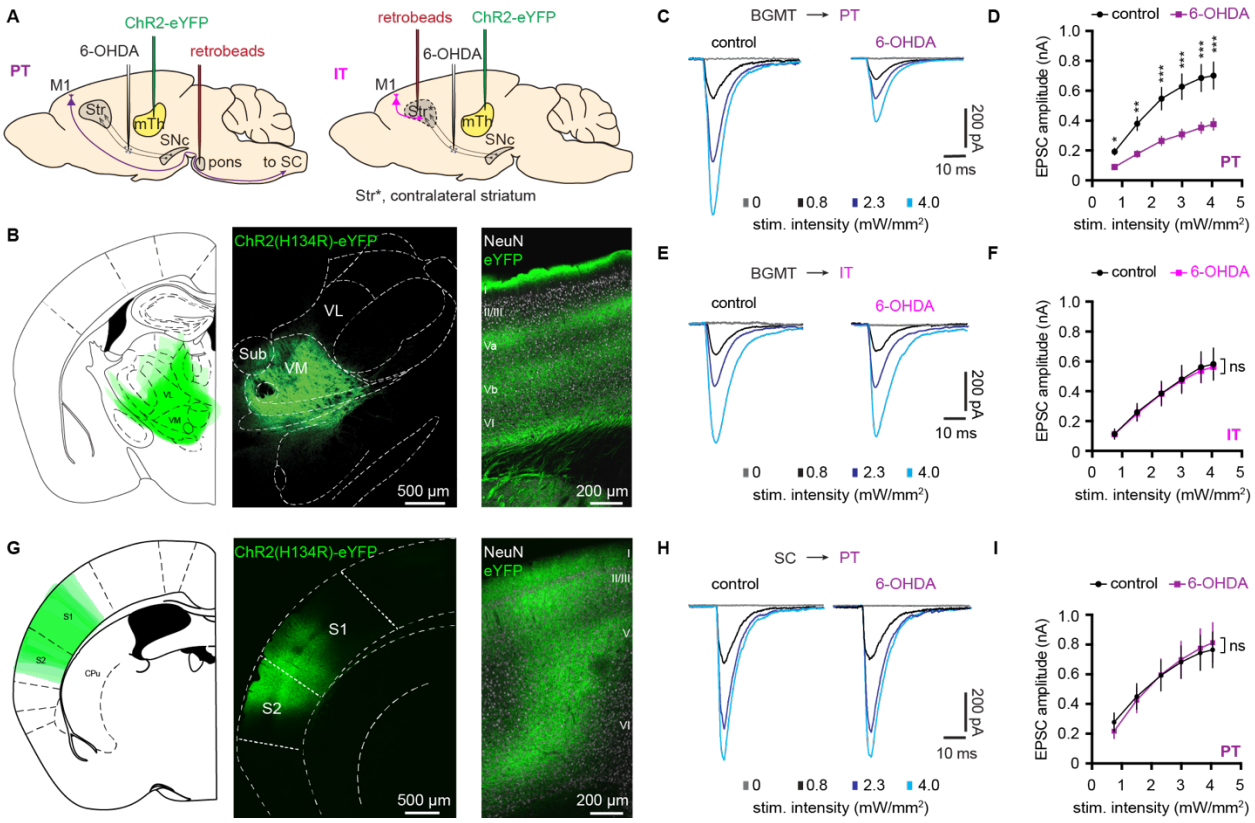


**Figure 1. SNc DA degeneration induces cell-subtype- and input-specific alterations in M1. A**) Schematic of overall strategies to retrogradely label M1 pyramidal neurons based on their projections and AAV-mediated optogenetics to selectively activate thalamocortical transmission arising from the motor thalamus (mTh) of both controls and 6-OHDA mice. **B**) AAV-infected areas were overlaid to show the centered AAV injection sites in the VM/VAL thalamus (left) and representative confocal image showing AAV9-ChR2(H134R)-eYFP infusion site in the ventral thalamus (middle), and eYFP-expressing thalamic axon terminals in the M1 of a mouse (right). eYFP-labeled terminals concentrate in the layers I and V and are consistent with the overall pattern of motor thalamic innervation of M1 in rodents. **C-D**) Representative traces of optogenetically-evoked EPSCs across different stimulation intensities in PT neurons from controls and 6-OHDA mice (**C**) and the summarized results (**D**). $P < 0.0001$ between groups, mixed effects model followed by Sidak's tests. *, $p < 0.05$, **, $p < 0.01$, ***, $p < 0.001$ relative to controls. Control = 62 cells/7 mice; 6-OHDA = 73 cells/8 mice. **E-F**) Representative traces of optogenetically-evoked EPSCs across different stimulation intensities in IT neurons from both controls and 6-OHDA mice (**E**) and the summarized results (**F**). ns, not significant between groups, mixed effects model. 26 cells/3 mice for each group. **G**) AAV-infected cortical regions were overlaid to show the center of AAV injections across animals (left) and representative confocal images showing AAV9-ChR2(H134R)-eYFP infusion site in the sensory cortical areas (middle), and eYFP-expressing cortical axon terminals in the M1 (right). **H-I**) Representative traces of optogenetically-evoked EPSCs arising from the SC across different stimulation intensities in M1 PT neurons from both controls and 6-OHDA mice (**H**) and the summarized results (**I**). Control = 20 cells/3 mice, 6-OHDA = 26 cells/3 mice. Mixed effects model, ns, not significant between groups.

**SNc DA degeneration induces cell-subtype- and input-specific alterations in M1**

To interrogate synaptic properties of thalamocortical inputs to projection-defined subtypes of M1 L5 pyramidal neurons in controls and 6-OHDA mice, (1) AAV9-hSyn-ChR2(H134R)-eYFP were injected into the BGMT, mainly targeting the VAL and VM thalamus (**Fig. 1A, B**); (2) Retrobeads were stereotaxically injected into the ipsilateral pontine nuclei and contralateral striatum to label PT and IT neurons, respectively (**Figure 1A**). Three weeks post-injection, intense eYFP labeled fibers could be observed, particularly in the layers I and V of M1 (**Figure 1B**) (*10*, *31*). Synaptic strength of thalamic inputs to PT and IT neurons was measured as the amplitude of optogenetically-evoked excitatory postsynaptic currents (oEPSCs) using *ex vivo* electrophysiology from controls and 6-OHDA mice.

Whole-cell voltage-clamp recordings were conducted in the presence of TTX (1 μM) and 4-AP (100 μM) to prevent the recruitment of polysynaptic responses and facilitate optogenetically evoked glutamate release from thalamic axon terminals (*10*, *32*). The amplitude of thalamic oEPSCs in M1 PT neurons was greatly reduced in slices from 6-OHDA mice relative to those from controls across a range of stimulation intensities (**Figure 1C, D**). In contrast, the amplitude of oEPSCs in the IT neurons was similar between 6-OHDA mice and controls (**Figure 1E, F**). These data suggest that chronic SNc DA degeneration selectively decreases synaptic strength of the motor thalamic excitation to M1 PT neurons.

Cerebral cortical neurons are equipped with a battery of homeostatic mechanisms that scale-up or -down synaptic strength to compensate for external perturbations (*33*). Thus, we examined whether SNc DA degeneration decreases global excitation to PT

neurons through homeostatic plasticity processes, or selectively decreases thalamic inputs? To answer this question, AAV-hSyn-ChR2(H134R)-eYFP were injected into the sensory cortical (SC) regions (**Figure 1G**) and retrobeads were injected into the pons to retrogradely label PT neurons. We found that the amplitude of oEPSCs from SC to PT neurons (SC-PT) was not altered between 6-OHDA mice and controls (**Figure 1H, I**). These data suggest that DA degeneration induces input-specific synaptic changes to M1 PT neurons. Together, chronic DA degeneration triggers cell-subtype- and input-specific adaptions in M1 local circuits.

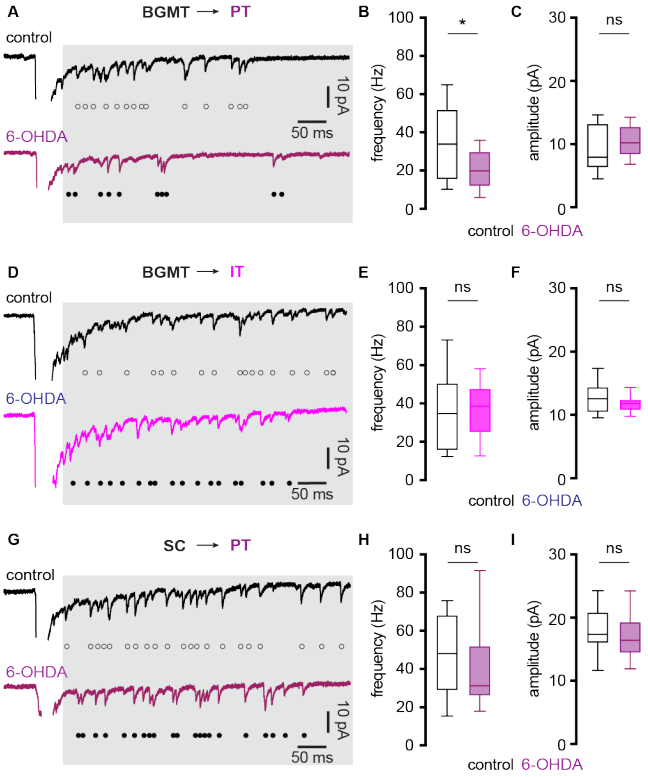

**Figure 2. SNc DA degeneration decreases the number of functional thalamic inputs to PT neurons. A**) Representative traces showing optogenetically-evoked, $Sr^{2+}$-induced asynchronous thalamocortical EPSCs of PT neurons from controls and 6-OHDA mice. Open and filled circle indicate individual events of asynchronous EPSCs. **B-C**) Box plots showing a reduced frequency (B, controls = 34 [15.5–52] Hz, n = 20 neurons/3 mice; 6-OHDA = 20 [12–30] Hz, n = 20 neurons/4 mice; $p$ = 0.02, MWU;) and unaltered amplitude (C, controls = 7.95 [6.3–13.2] pA, n = 20 neurons/3 mice; 6-OHDA = 10.2 [8.4–12.8] pA, n = 20 neurons/4 mice; $p$ = 0.33, MWU) of $Sr^{2+}$-EPSCs at thalamic inputs to M1 PT neurons from 6-OHDA mice relative to controls. **D**) Representative traces showing optogenetically-evoked, $Sr^{2+}$-induced quantal EPSCs of thalamic inputs to IT neurons from controls and 6-OHDA mice. Open and filled circle indicate individual events of asynchronous EPSCs. **E-F**) Box plots showing unaltered frequency (E, controls = 34.8 [15.7–50.5] Hz, n = 22 neurons/3 mice; 6-OHDA = 38.4 [24.9–47.6] Hz, n = 22 neurons/3 mice; $p$ = 0.7, MWU) and amplitude (F, control = 12.6 [10.5–14.4] pA; 6-OHDA = 11.8 [10.8–12.4] pA; n = 22 neurons/3 mice; $p$ = 0.34, MWU;) of $Sr^{2+}$-EPSCs at thalamic inputs to IT neurons between groups. **G**) Representative traces showing optogenetically-evoked, $Sr^{2+}$-induced quantal EPSCs of sensory cortical inputs to PT neurons from controls and 6-OHDA mice. Open and filled circles indicate individual events of asynchronous EPSCs. **H-I**) Box plots showing unaltered frequency (H, controls = 48 [29–68] Hz, n = 20 neurons/3 mice; 6-OHDA = 31.2 [26–52] Hz, n = 19 neurons/3 mice; $p$ = 0.6, MWU) and amplitude (I, control = 17 [16–20.8] pA, n = 20 neurons/3 mice; 6-OHDA = 16.5 [14.4–19.3] pA, n = 19 neurons/3 mice; $p$ = 0.5, MWU) of $Sr^{2+}$-EPSCs at sensory cortical inputs to M1 PT neurons between groups. ns, not significant.

## SNc DA degeneration decreases the number of functional thalamic inputs to PT neurons

To gain mechanistic understanding of synaptic adaptations of M1 circuits following the loss of SNc DA neurons, we assessed the quantal properties of glutamatergic neurotransmission to PT and IT neurons in M1 (*31*, *34*, *35*). Replacing extracellular $Ca^{2+}$ with $Sr^{2+}$ (2 mM), we found a significantly reduced frequency, but an unaltered amplitude, of optogenetically-evoked thalamic asynchronous EPSCs ($Sr^{2+}$-EPSCs) in PT neurons from 6-OHDA mice relative to those from controls (**Figure 2A-C**). In contrast, neither the frequency nor the amplitude of thalamic $Sr^{2+}$-EPSCs in IT neurons was altered in 6-OHDA mice relative to controls (**Figure 2D-F**). Consistent with the intact synaptic strength of sensory cortical inputs to PT neurons (**Figure 1G-I**), neither the frequency nor the amplitude of $Sr^{2+}$-EPSCs at SC–PT synapses was altered by DA depletion (**Figure 2G-**

**I**). These data further support that SNc DA degeneration selectively affects thalamic projection to PT neurons, largely due to fewer functional BGMT-PT connections.

**SNc DA degeneration induces structural changes of thalamocortical synapses to PT neurons**

To assess how loss of DA alters thalamocortical innervation of M1 PT neurons, brain sections from control and 6-OHDA mice were processed for immunohistochemical detection of vesicular glutamate transporter 2 (vGluT2), a marker of thalamic axon boutons in M1. Stereological methods were used to quantify vGluT2-immunoreactive (vGluT2-ir) puncta in the layer V of M1. Consisted with findings from MPTP-treated NHP (*24*), the density of vGluT2-ir puncta in the L5 was significantly decreased in slices from 6-OHDA mice relative to those from controls (**Figure 3A-C**). These data suggest that DA depletion likely induces a loss of presynaptic thalamic axon terminals in M1, though a potential decrease in vGluT2 expression cannot be excluded.

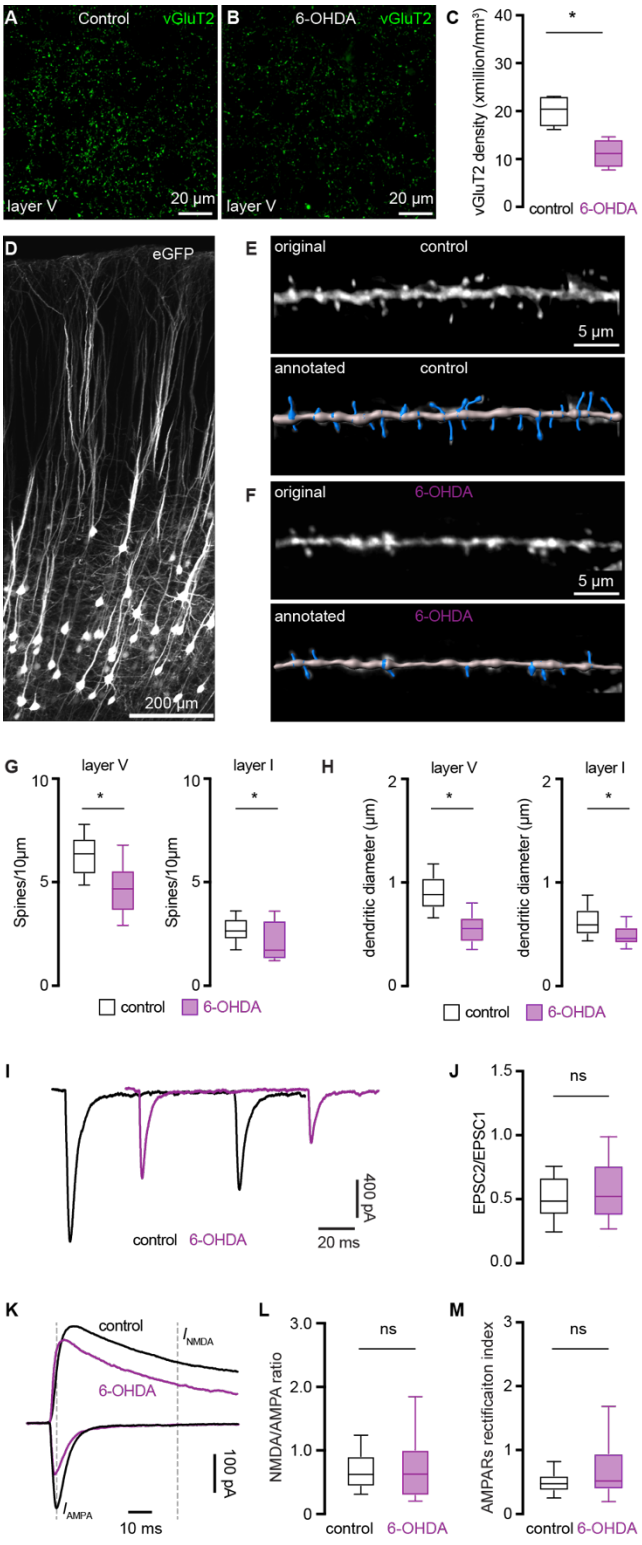
A
Control
vGluT2
layer V
20 µm
B
6-OHDA
vGluT2
layer V
20 µm
C
vGluT2 density (xmillion/mm³)
40
30
20
10
0
*
control
6-OHDA
D
eGFP
200 µm
E
original
control
5 µm
annotated
control
F
original
6-OHDA
5 µm
annotated
6-OHDA
G
layer V
layer I
Spines/10µm
10
5
0
*
control
6-OHDA
H
layer V
layer I
dendritic diameter (µm)
2
1
0
*
control
6-OHDA
I
400 pA
control
6-OHDA
20 ms
J
EPSC2/EPSC1
1.5
1.0
0.5
0.0
ns
K
control
$I_{NMDA}$
6-OHDA
100 pA
$I_{AMPA}$
10 ms
L
NMDA/AMPA ratio
3.0
2.0
1.0
0
ns
control
6-OHDA
M
AMPARs rectificaiton index
3
2
1
0
ns
control
6-OHDA

**Figure 3**. **SNc DA degeneration alters the structure of thalamocortical synapses to PT neurons**. **A-C**) Representative confocal images of vGluT2-immunoreactivity in the layer 5 of M1 from controls (A) and 6-OHDA mice (B), and the summarized results showing a reduced vGluT2 density in the layer 5 of M1 following the SNc DA degeneration (**C**, control = 20.4 [16.9–22.9] million puncta/mm$^3$, n = 20 slices/3 mice; 6-OHDA = 11.2 [8.5–13.9] million puncta/mm$^3$, n = 20 slices/3 mice; $p < 0.0001$, MWU). **D-E**) Representative confocal images of eGFP-labeled PT neurons in M1 (D) and segments of basal dendrites from controls (E) and 6-OHDA mice (F). Original dendrites and spines (upper panels in E, F) were annotated using Imaris software (lower panel in E, F) for quantification. **G**) Summarized results showing decreased spine densities of L5 basal dendrites (control = 6.4 [5.4–7.1] per 10 µm, n = 53 segments/3 mice; 6-OHDA = 4.7 [3.6–5.5] per 10 µm, n = 47 segments/3 mice; $p < 0.001$, MWU) and L1 apical dendrites (controls = 2.6 [2.3–3.2] per 10 µm, n = 24 segments/3 mice; 6-OHDA = 1.7 [1.3–3.1] per 10 µm, n = 25 segments/3 mice; $p = 0.02$, MWU). **H**) Summarized results showing reduced dendritic diameters of L5 basal dendrites (control = 0.9 [0.77–1.06] µm, n = 262 samples/3 mice; 6-OHDA = 0.57 [0.44–0.67], n = 267 samples/3 mice; $p < 0.0001$, MWU) and L1 apical dendrites (control = 0.59 [0.5–0.74] µm, n = 240 samples/3 mice; 6-OHDA = 0.46 [0.42–0.57], n = 240 samples/3 mice; $p < 0.0001$; MWU) from 6-OHDA mice, relative to controls. **I-J**) Representative traces of EPSCs in response to paired pulses stimulation from controls and 6-OHDA mice (I) and the summarized results showing unaltered paired-pulse ratios between groups (J, control = 0.49 [0.39–0.66], n= 62 neurons/7 mice; 6-OHDA = 0.52 [0.38–0.75], n = 73 neurons/8 mice; $p = 0.1$, MWU). **K-M**) Representative traces of optogenetically-evoked thalamic EPSCs recorded at -80 mV and +40 mV in PT neurons from controls and 6-OHDA mice. Dashed lines in (K) indicate where AMPARs- and NMDARs-mediated responses were measured to quantify NMDA/APMA ratio (L) and AMPARs rectification (M). Summarized results showing no change in the NMDA/AMPA ratio (L, control = 0.62 [0.44–0.91], n = 34 neurons/4 mice; 6-OHDA = 0.63 [0.29–1.0], n = 38 neurons/5 mice; $p = 0.85$, MWU) and AMPARs rectification index (M, control = 0.47 [0.37–0.6], n = 34 neurons/4 mice; 6-OHDA = 0.52 [0.39–0.94], n = 38 neurons/5 mice; $p = 0.22$, MWU) between groups.

Thalamic axon terminals innervate the dendritic spines and dendritic shaft in the L1 and L5 of M1 pyramidal neurons (*5*, *10*, *24*). To interrogate postsynaptic structural changes associated with DA depletion, the density of dendritic spines and the diameter of dendritic shaft of retrogradely labeled M1 PT neurons were assessed in slices from controls and 6-OHDA mice that received AAVrg-hSyn-eGFP injections into the pontine nuclei (**Figure 3D, F**). Density of basal dendritic spines in the layer V from 6-OHDA mice decreased significantly relative to those from controls (**Figure 3E-G**). Similarly, the densities of eGFP-labeled spines on the L1 apical dendrites also decreased significantly in slices from 6-OHDA mice relative to those from controls (**Figure 3G**). Further, the diameters of both L5 basal dendrites and L1 apical dendrites were decreased significantly

in 6-OHDA mice relative to controls (**Figure 3H**). The above data suggest that SNc DA degeneration induces loss of dendritic spines and shrunk dendritic shafts of PT neurons. The decreased presynaptic vGluT2 density and postsynaptic morphological changes support that degeneration of SNc DA neurons induces functional impairments of thalamocortical synapses to M1 PT neurons.

**SNc DA degeneration does not alter postsynaptic receptor properties of thalamocortical synapses to M1 PT neurons**

Next, we assessed functional adaptations at thalamocortical inputs to M1 PT neurons following the loss of SNc DA neurons. There was no significant change in the paired pulse ratio (PPR) of thalamocortical oEPSCs in PT neurons from controls and 6-OHDA mice (**Figure 3I, J**). It suggests that the decreased thalamocortical projection to PT neurons was not due to a lower initial release probability at thalamic axon terminals.

To assess postsynaptic adaptations at thalamocortical synapses to PT neurons, we measured the ratio of EPSCs mediated by NMDA receptors (Rs) and AMPARs (NMDA/AMPA ratio) as well as AMPARs rectification properties between controls and 6-OHDA mice. There was no difference in the NMDA/AMPA ratio at thalamic projections to PT neurons between groups (**Figure 3K, L**). Moreover, there was no alteration in the inward rectification index of AMPARs at thalamic projections to PT neurons (**Figure 3K, M**). These data suggest that SNc DA degeneration does not alter the composition of postsynaptic glutamatergic receptors at thalamocortical synapses to PT neurons.

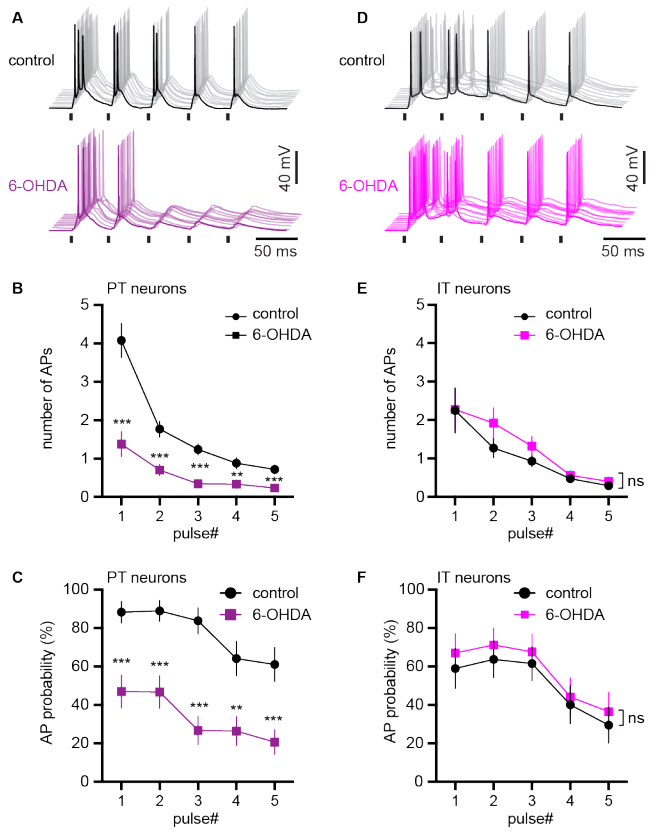


**Figure 4**. **SNc DA degeneration decreases the effectiveness of thalamic driving of M1 PT neuronal firing**. **A**) Representative traces of AP firing of M1 PT neurons from controls and 6-OHDA mice in response to 20 Hz optogenetic stimulation. AP traces from 10 trials were aligned for both groups. **B-C**) Summarized results show that both the number (B) and probability (C) of synaptically-generated APs in M1 PT neurons decreased significantly in 6-OHDA mice relative to controls. Mixed effects model followed by Sidak's tests, $p < 0.0001$ for group difference. Control = 29 neurons/3 mice; 6-OHDA = 33 neurons/4 mice. **D**) Representative traces of AP firing of M1 IT neurons from controls and 6-OHDA mice in response to 20 Hz optogenetic stimulation. **E-F**) Summarized results show that the number (E) and probability (F) of synaptically-generated APs in M1 IT neurons was not altered in 6-OHDA mice relative to controls. Mixed effects model, $p = 0.56$ for group difference on AP probability; $p = 0.36$ for group difference on the number of APs; control = 19 neurons/3 mice; 6-OHDA = 17 neurons/3 mice.

## SNc DA degeneration decreases the effectiveness of thalamic driving of M1 PT neuronal firing

An enhanced synchronized β band bursting pattern of thalamocortical activity observed in parkinsonian state (*16*, *36*, *37*). It is plausible to hypothesize that thalamic inputs drive the aberrant thalamocortical synchronization through the altered dendritic excitability,

which cannot be accurately measured using whole-cell voltage-clamp recordings. To test this hypothesis, we recorded retrogradely labeled PT and IT neurons under current-clamp mode and assess the effectiveness of thalamic inputs in driving neuronal firing in both control and 6-OHDA mice. A 20-Hz optogenetic stimulation (1 ms duration) was delivered to activate ChR2-tagged thalamic axons in M1. Interestingly, the effectiveness of thalamic driving of PT neuronal firing decreased significantly in slices from 6-OHDA mice relative to those from controls, as reflected by fewer APs per stimulation and a decreased AP firing probability (**Figure 4A-C**). In contrast, we did not detect alterations in the effectiveness of thalamic driving of IT neuronal firing between groups (**Figure 4D-F**). Consistent with the weakened thalamic inputs to PT neurons, these data suggest that loss of DA selectively disrupts the effectiveness of thalamic drive of PT neurons to fire APs. The results also suggest that monosynaptic thalamic inputs are not sufficient to synchronize PT neuronal firing in bursts under parkinsonian state (see Discussions).

To determine the relative contributions of AMPARs- and NMDARs-mediated responses to thalamic driving of PT neurons firings, pharmacological approach was used to assess the impact of NMDARs and AMPARs blockade on the number of synaptically generated APs from PT neurons in control mice. The number of APs generated by PT neurons in response to optogenetic stimulation of thalamic axon terminals was significantly reduced by blockade of NMDARs using D-APV (50 μM), particularly the number of APs generated by the first two stimulations (**Supplementary figure 1**). Synaptically generated APs of PT neurons were abolished by the subsequent blockade of both NMDARs and AMPARs using a mixture of D-APV (50 μM) and DNQX (20 μM)

(**Supplementary figure 1**). These data suggest that NMDARs of PT neurons play a significant role in mediating thalamus-driven AP firing in physiological state.

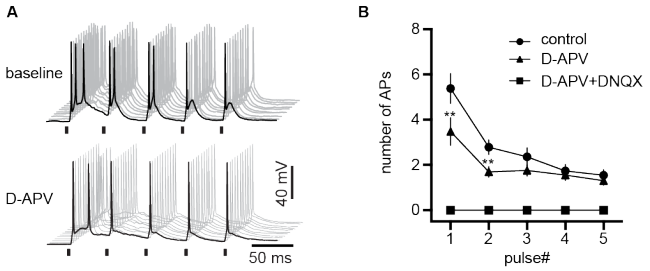


**Supplementary figure 1**. NMDARs and AMPARs mediate thalamic drive of PT neurons to fire in control mice. **A**) Representative traces of AP firing of M1 PT neurons in response to 20 Hz optogenetic stimulation prior to and after D-APV application. **B**) Summarized results show that NMDARs blockade using D-APV decreased the number of thalamus-driven APs of PT neurons. **, $p < 0.01$, mixed effects model followed by Sidak's tests; 13 neurons/3 mice.

**Distinct composition of glutamatergic receptors at thalamic and sensory cortical inputs to M1 PT neurons**

NMDA receptors play a critical role in thalamocortical synaptic integration and plasticity and contribute to pathological adaptations in neurological disorders (*23*, *38*, *39*). Next, we tested the hypothesis that NMDARs at thalamocortical synapses mediate the selective downregulation of thalamic excitation of PT neurons in parkinsonian state.

To do this, we first measured the NMDA/AMPA ratio at thalamic projections to PT and IT neurons (i.e., BGMT-PT and BGMT-IT synapses, respectively) as well as sensory cortical synapses to PT neurons (i.e., SC-PT synapse) in controls. Interestingly, we found a significantly higher NMDA/AMPA ratio at the BGMT-PT synapses, relative to BGMT-IT synapses and SC-PT synapses (**Figure 5A, B**). These data indicate that NMDARs are functionally enriched at BGMT-PT synapses relative to SC-PT or BGMT-IT synapses. In addition, there was a stronger inward rectification of AMPARs at SC-PT synapses relative to thalamic projections to PT or IT neurons (**Figure 5A, C**). These data indicate that

GluA2-lacking, $Ca^{2+}$-permeable AMPARs are enriched at SC-PT synapses relative to those from the motor thalamus to M1 PT or IT neurons in control mice.

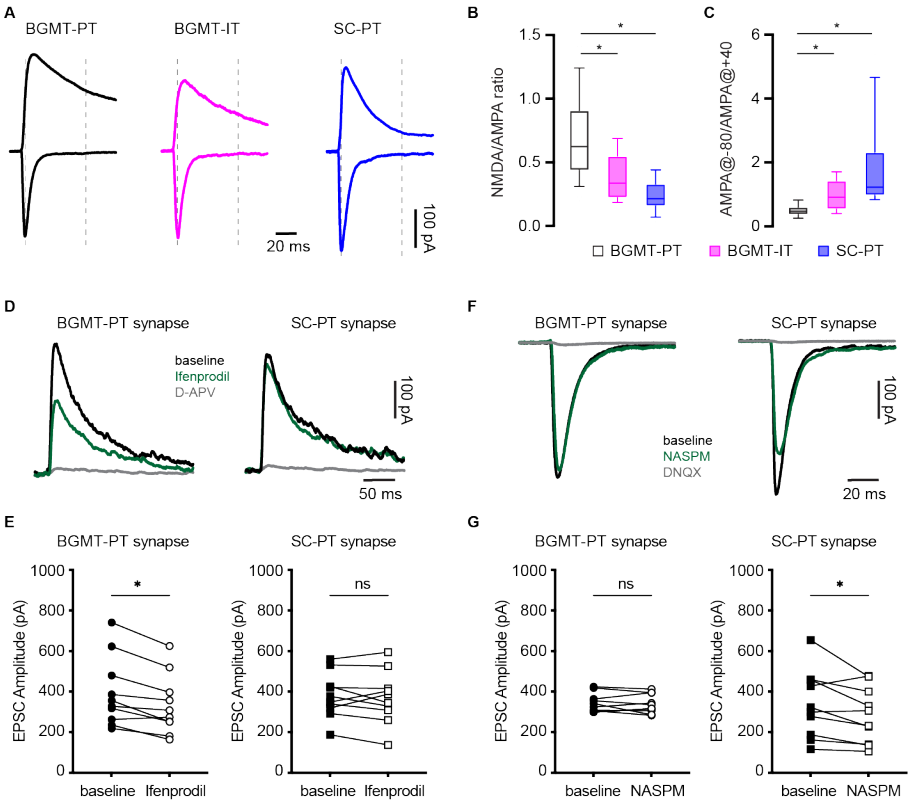

**Figure 5**. **Distinct postsynaptic receptor properties at thalamic and sensory cortical inputs to PT neurons**. **A**) Representative traces of AMPARs- and NMDARs-mediated responses from different synapses in M1. **B-C**) Box plots showing difference in the NMDA/AMPA ratios (**B**, BGMT-PT synapses = 0.62 [0.44–0.91], n = 34 neurons/4 mice; BGMT-IT synapse = 0.34 [0.22–0.55], n = 19 neurons/3 mice; SC-PT synapses = 0.22 [0.16–0.33], n = 25 neurons/3 mice; $p < 0.0001$; Kruskal-Wallis test followed by Dunn's test) and AMPARs rectification properties (**C**, BGMT-PT synapses = 0.47 [0.37–0.60], n = 34 neurons/4 mice; BGMT-IT synapse = 0.91 [0.54–1.4], n = 25 neurons/3 mice; SC-PT synapses = 1.23 [0.97–2.32], n = 19 neurons/3 mice; $p < 0.0001$; Kruskal-Wallis test followed by Dunn's test) of different synapses in M1. **D-E**) Pharmacology studies showing different sensitivities of NMDARs-mediated transmission at thalamic and sensory cortical synapses to ifenprodil. **D**) Representative traces of isolated NMDARs-mediated EPSCs from BGMT-PT and SC-PT synapses at baseline, in ifenprodil, and in ifenprodil plus D-APV. **E**) Connected symbols showing the effects of ifenprodil to the amplitude of NMDARs-mediated EPSCs at BGMT-PT (left, baseline = 342 [256–516] pA, ifenprodil = 292 [234–428] pA; n = 10 neurons/4 mice; $p = 0.004$, WSR) and SC-PT (right, baseline = 363 [313–452] pA, ifenprodil = 366 [296–443] pA; n = 10 neurons/3 mice; $p = 0.6$, WSR) synapses. **F**) Representative traces of AMPARs-mediated EPSCs from BGMT-PT and SC-PT synapses at baseline, in NASPM, and in NASPM plus DNQX. **G**) Connected symbols showing the effects of NASPM to the amplitude of AMPARs-mediated EPSCs at BGMT-PT (left, baseline = 333 [305–378] pA; NASPM = 327 [301–395] pA; n = 10 neurons/ 4 mice; $p = 0.6$, WSR) and SC-PT synapses (right, baseline = 311 [181–459] pA; NASPM = 269 [106–419] pA; n = 10 neurons/ 4 mice; $p = 0.02$, WSR).

Next, pharmacological approach was used to further confirm the input-specific composition of glutamatergic receptors in PT neurons. A large body of evidence suggests that GluN2B subunit-containing NMDA receptors with larger $Ca^{2+}$ conductance enriched at thalamocortical synapses in the prefrontal cortex and play a critical role in pathological processes in neurological diseases (*38*, *40*). Consistently, a noncompetitive antagonist of GluN2B-containing NMDARs ifenprodil (3 μM) significantly and consistently reduced the amplitude of NMDARs-EPSCs at BGMT-PT synapses, but not did not produce consistent effect to the NMDARs-EPSCs amplitude of SC-PT synapses (**Figure 5D, E**). In addition, to quantitively assess the functional contribution of GluA2-lacking, $Ca^{2+}$-permeable AMPARs at different inputs, a selective antagonist 1-Naphthyl acetyl spermine trihydrochloride (NASPM) was used. Bath application of NASPM (100 μM) consistently decreased the amplitude of AMPARs-EPSCs of SC-PT synapses but did not produce significant effect to AMPARs-EPSCs at BGMT-PT synapses (**Figure 5F, G**).

Together, we conclude that GluN2B-containing NMDARs are enriched at BGMT-PT synapses, and that GluA2-lacking, $Ca^{2+}$-permeable AMPARs functionally contribute more to sensory cortical transmission to PT neurons in physiological state.

**NMDARs mediate the decreased thalamocortical transmission to M1 PT neurons**

Activation of NMDARs by exogenously application of NMDA is sufficient to mimic NMDAR-dependent pathological processes in basal ganglia nuclei of parkinsonian animals (*34*, *41*). Given the enrichment of NMDARs at BGMT-PT synapses, we further assessed if NMDARs activation mediates the decreased thalamocortical synaptic strength to PT neurons in parkinsonian state. To do this, brain slices were treated with exogenous NMDA (25 μM) for 1 hour followed by anatomical and physiology studies. Our earlier studies showed that this treatment protocol did not induce degeneration of glutamatergic neurons in brain slices (*34*). Specifically, brain slices from controls and 6-OHDA mice were incubated with (1) normal ACSF, (2) NMDA-containing ACSF (25 μM), or (3) D-APV/NMDA-containing ACSF for one hour (*34*), prior to physiological and anatomical studies (**Figure 6A**). In brain slices from vehicle-injected control mice, NMDA incubation *ex vivo* reduced the amplitude of thalamic oEPSCs of PT neurons (**Figure 6B, D**), and the effects of NMDA could be abolished by D-APV co-incubation (**Supplementary figure 2**). If activation of NMDARs *in vivo* contributes to the reduced thalamic excitation to PT neurons in parkinsonian state, a corollary would be that the effects of NMDARs activation to thalamic oEPSCs *ex vivo* (**Figure 6B, D**) should be occluded in slices from 6-OHDA mice. Consistently, *ex vivo* NMDA incubation had no effect to the amplitude of thalamic oEPSCs of PT neurons from 6-OHDA mice (**Figure 6C, E**). These data suggest that excessive NMDARs activation is sufficient to decrease

the thalamic excitation to PT neurons from control mice, and such effect likely mediates the reduced thalamic excitation to PT neurons *in vivo* following DA depletion.

Loss of DA decreases the number of functional thalamocortical connections to PT neurons (**Figures 2 & 3**). Thus, we further studied the impact of exogenous NMDA incubation on $Sr^{2+}$-induced quantal glutamate release at thalamocortical synapses to PT neurons. In slices from vehicle-injected controls, NMDA incubation significantly decreased the frequency, but not the amplitude of optogenetically evoked thalamic $Sr^{2+}$-EPSCs (**Figure 6F, G**). In contrast, in slices from 6-OHDA mice, NMDA incubation did not alter the frequency or the amplitude of optogenetically-evoked thalamic $Sr^{2+}$-EPSCs of PT neurons (**Figure 6H, I**). The above data suggest that NMDARs activation reduces the number of functional thalamocortical inputs to M1 PT neurons, but this effect was occluded in 6-OHDA mice.

Next, we studied whether *ex vivo* NMDA incubation could induce structural changes at thalamocortical synapses to PT neurons. A separate set of brain slices from controls and 6-OHDA mice were incubated with ACSF or NMDA-containing ACSF for 1 hour and then fixed with 4% PFA for immunohistochemistry studies. We found that *ex vivo* NMDA incubation robustly decreased vGluT2 densities in the L5 of M1 of controls, relative to those incubated in ACSF (**Figure 6J, K**). However, NMDA incubation did not alter vGluT2 densities in the L5 of M1 from 6-OHDA mice relative to those treated with normal ACSF (**Figure 6L, M**). Postsynaptically, NMDA incubation decreased the spine densities of L5 basal dendrites of retrogradely labeled PT neurons from controls (**Figure 6N, O**); but NMDA incubation did not alter spine densities of PT neurons from 6-OHDA mice (**Figure 6P, Q**). Altogether, our physiological and anatomical results suggest that

excessive NMDARs activation is sufficient to decrease thalamocortical connection to M1 PT neurons, and that the NMDA-mediated mechanisms likely underlie the decreased thalamic excitation to PT neurons in 6-OHDA mice.

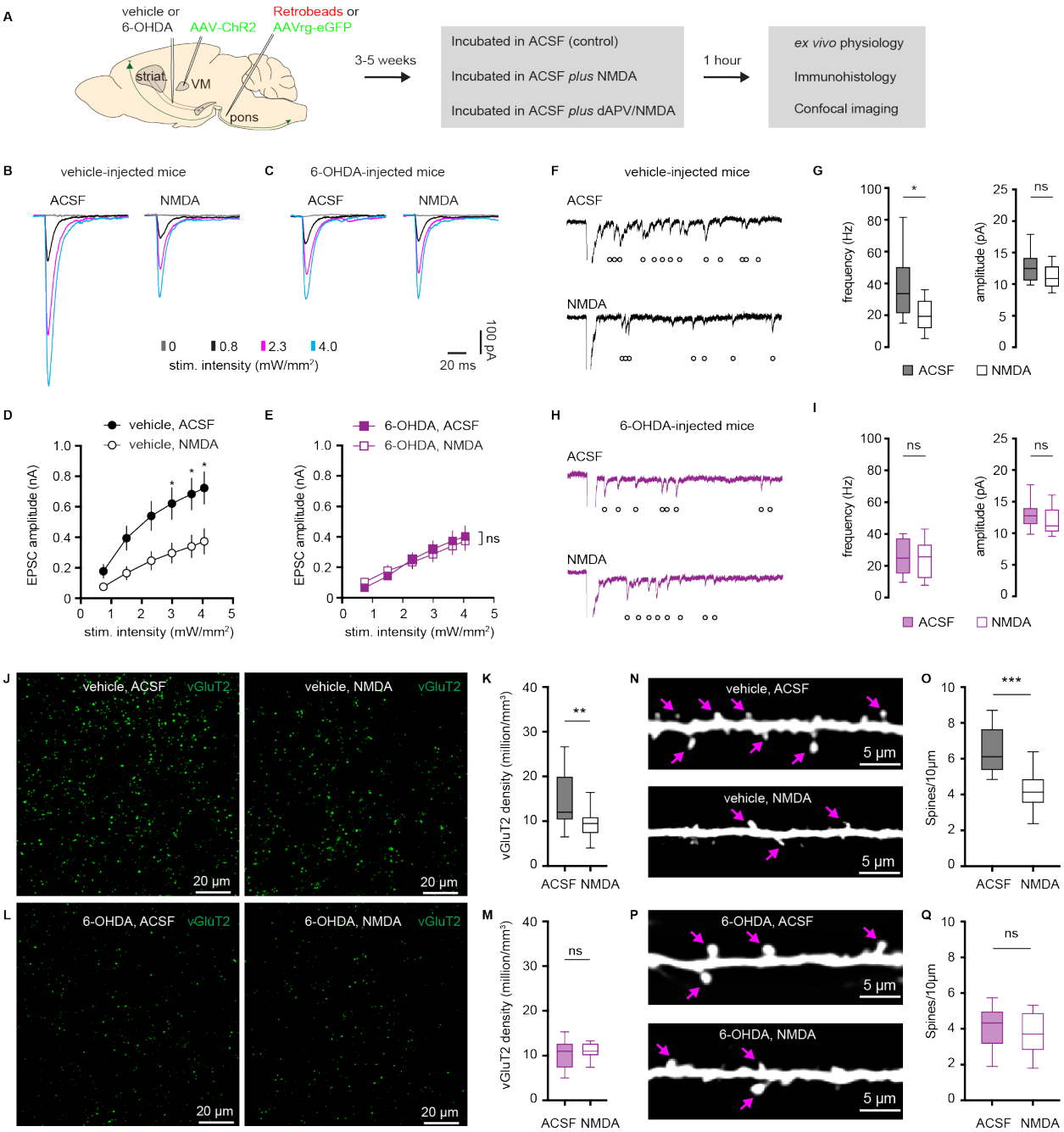

**Figure 6**. **Excessive NMDARs activation mediates the impaired thalamocortical transmission after DA depletion**. **A**) Experimental design. **B-C**) Representative traces of optogenetically-evoked thalamocortical EPSCs of PT neurons from vehicle-injected controls (B) and 6-OHDA-injected mice (C), which were either incubated in normal ACSF (control) or ACSF containing NMDA. **D-E**) Summarized results show that NMDA incubation decreased the amplitude of oEPSCs from vehicle-injected controls (D, group effect, $p < 0.0001$, mixed effects model followed by Sidak's tests), but not those from 6-OHDA-injected mice (E, group effect, $p > 0.79$, mixed effects model). **F-G**) NMDA incubation decreased the frequency but not the amplitude of optogenetically-evoked $Sr^{2+}$-EPSCs from vehicle-injected controls. **F**) Representative traces of $Sr^{2+}$-EPSCs. **G**) Summarized results (frequency of $Sr^{2+}$-EPSCs in vehicle-injected mice, control = 33.6 [21.1–50.4] Hz, n = 24 neurons/3 mice; NMDA = 10.9 [9.6–12.9] pA; n = 24 neurons/3 mice; $p = 0.001$, MWU; amplitude of $Sr^{2+}$-EPSCs in vehicle-injected mice, control = 12.5 [10.5–14.2] pA, n = 24 neurons/3 mice; NMDA = 19.4 [11.8–29.2] Hz, n = 24 neurons/3 mice; $p = 0.1$, MWU). **H-I**) NMDA incubation did not alter the frequency or the amplitude of optogenetically-evoked $Sr^{2+}$-EPSCs from 6-OHDA-injected mice. **H**) Representative traces of $Sr^{2+}$-EPSCs. **I**) Summarized results (frequency of $Sr^{2+}$-EPSCs in 6-OHDA mice, control = 24.8 [15–37.4] Hz, n = 17 neurons/3 mice; NMDA = 25.6 [12.2–33.4] pA, n = 17 neurons/3 mice; $p = 0.6$, MWU; amplitude of $Sr^{2+}$-EPSCs in 6-OHDA mice; control = 12.9 [11.3–14.0] pA, n = 17 neurons/3 mice; NMDA = 11.2 [10.3–13.8] Hz, n = 27 neurons/3 mice; $p = 0.21$, MWU). **J**) Representative confocal images of vGluT2 immunoreactivity from ACSF- and NMDA-treated slices of controls. **K**) Box plot shows that NMDA incubation reduced vGluT2 densities in slices of controls (ACSF = 12 [10–14.8] million/$mm^3$, n = 20 samples/3 mice; NMDA = 9 [7–10.8] million/$mm^3$, n = 16 samples/3 mice; $p = 0.0016$, MWU). **L**) Representative confocal images of vGluT2 immunoreactivity from ACSF- and NMDA-treated slices of 6-OHDA. **M**) Box plot shows that NMDA incubation did not affect vGluT2 densities in slices of 6-OHDA mice (ACSF = 11 [8–12] million/$mm^3$, 20 samples/3 mice; NMDA = 11 [9–12] million/$mm^3$, 20 samples/3 mice; $p = 0.7$, MWU). **N**) Representative confocal images of M1 L5 dendritic spines from ACSF- and NMDA-treated slices of controls. **O**) Box plot shows that NMDA incubation reduced L5 spine densities in slices of controls (ACSF = 6 [5.4–7.6] spines/10 µm, n = 24 samples/3 mice; and NMDA = 4.1 [3.5–4.9] spines/10 µm, n = 25 samples/3 mice; $p < 0.0001$, MWU). **P**) Representative confocal images of M1 L5 dendritic spines from ACSF- and NMDA-treated slices of 6-OHDA mice. **Q**) Box plot shows that NMDA incubation did not alter L5 spine densities in slices from 6-OHDA mice (ACSF = 4.3 [3.2–5] spines/10 µm, n = 29 samples/3 mice; NMDA = 3.7 [2.8–4.9] spines/10 µm, n = 31 samples/3 mice; $p = 0.4$, MWU;). Arrows in (N and P) indicate representative spines on dendrites.

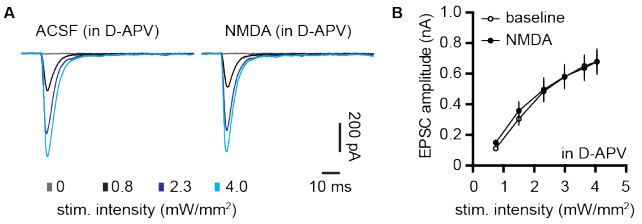


**Supplementary figure 2**. ***Ex vivo*** **NMDA receptor activation does not affect cellular excitability of M1 PT neurons**. **A**) Representative traces of action potentials of PT neurons from slices treated with normal ACSF (control) or ACSF containing NMDA (25 µM). **B**) Summarized data. Mixed effects model, $p > 0.05$.

Our recent work also showed that loss of DA decreases the intrinsic excitability of PT neurons (*26*). Whether the intrinsic and synaptic adaptations in PT neurons share the same NMDA-mediated mechanisms remain unknown. To address this question, we studied the impact of NMDA incubation on cellular excitability of M1 PT neurons from control mice. Interestingly, exogenous NMDA incubation did not alter the cellular excitability of PT neurons in slices from controls (**Supplementary figure 3**). The above data indicate chronic NMDARs activation was not sufficient or involved to trigger intrinsic adaptations in M1 PT neurons. Taken together, these data suggest that (1) NMDARs activation *ex vivo* was sufficient to decrease thalamocortical transmission in slice from control mice; (2) NMDARs-mediated reduction of thalamocortical transmission to PT neurons *ex vivo* was occluded after DA depletion; and (3) distinct molecular mechanisms mediate the intrinsic and synaptic adaptations of PT neurons after DA depletion.

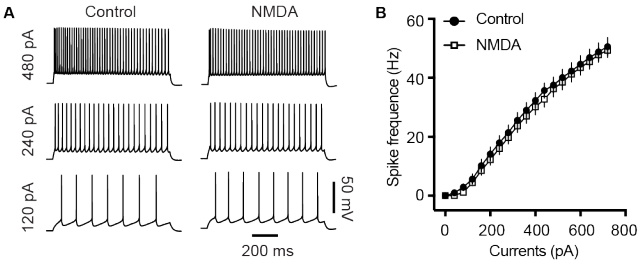


**Supplementary figure 3**. ***Ex vivo* NMDA receptor activation does not affect cellular excitability of M1 PT neurons**. **A**) Representative traces of action potentials of PT neurons from slices treated with normal ACSF (control) or ACSF containing NMDA (25 μM). **B**) Summarized data. Mixed effects model, $p > 0.05$.

## Basal ganglia outputs drive the decreased thalamocortical transmission in parkinsonian state

BG-thalamocortical network shows an exaggerated oscillatory and bursting pattern of activity in parkinsonian state (*2*, *36*). Recent studies suggests that propagation of synchronized oscillations to the BGMT, via BG GABAergic outputs, engages thalamic

neurons into synchronized rebound-burst firing (*16*, *37*, *42*, *43*). Such pathologic rebound excitation and cellular hyperexcitability in the BGMT could effectively entrain cortical activity, contributing to parkinsonian motor symptoms (*15*, *16*, *42–44*). Thus, it is likely that the enhanced glutamate release at thalamocortical axon terminals associated with the synchronized burst firing excessively activates NMDARs of PT neurons (*15*, *43*), further leading to the decreased thalamic input to PT neurons in parkinsonian state. Thus, a corollary would be that disruption of the abnormally synchronized bursting pattern of activity throughout BG-thalamocortical network would suppress the abnormal activation of cortical NMDARs and thus prevent the thalamocortical synaptic changes in parkinsonian state. Studies showed that intervention of SNr activity could effectively suppress propagation of pathological oscillations to the motor thalamus and the motor cortex (*16*, *37*). Thus, we employed chemogenetic approaches to suppress basal ganglia output *in vivo* to study its impact on M1 circuitry (dys)function in both controls and DA-depleted mice.

PV-Cre knock-in mice were used to selectively target parvalbumin (PV)-expressing GABAergic projection neurons in the SNr. These mice were unilaterally injected with vehicle or 6-OHDA into the MFB, plus AAV9-hSyn-FLEX-hM4Di-mCherry into the SNr of the same hemisphere for chemogenetic manipulation of basal ganglia outputs (**Figure 7A**). Immunofluorescence staining showed a selective expression of hM4Di (Gi)-DREADDS on SNr PV-expressing cells (**Figure 7A**). There was no difference in the number of hM4Di-expressing cells in the SNr between 6-OHDA mice and controls. Loose-sealed cell-attached recordings showed that bath application of DREADDS agonist CNO

(10 μM) effectively suppressed the frequency and regularity of autonomous firing of SNr neurons from 6-OHDA mice (**Figure 7C, D**).

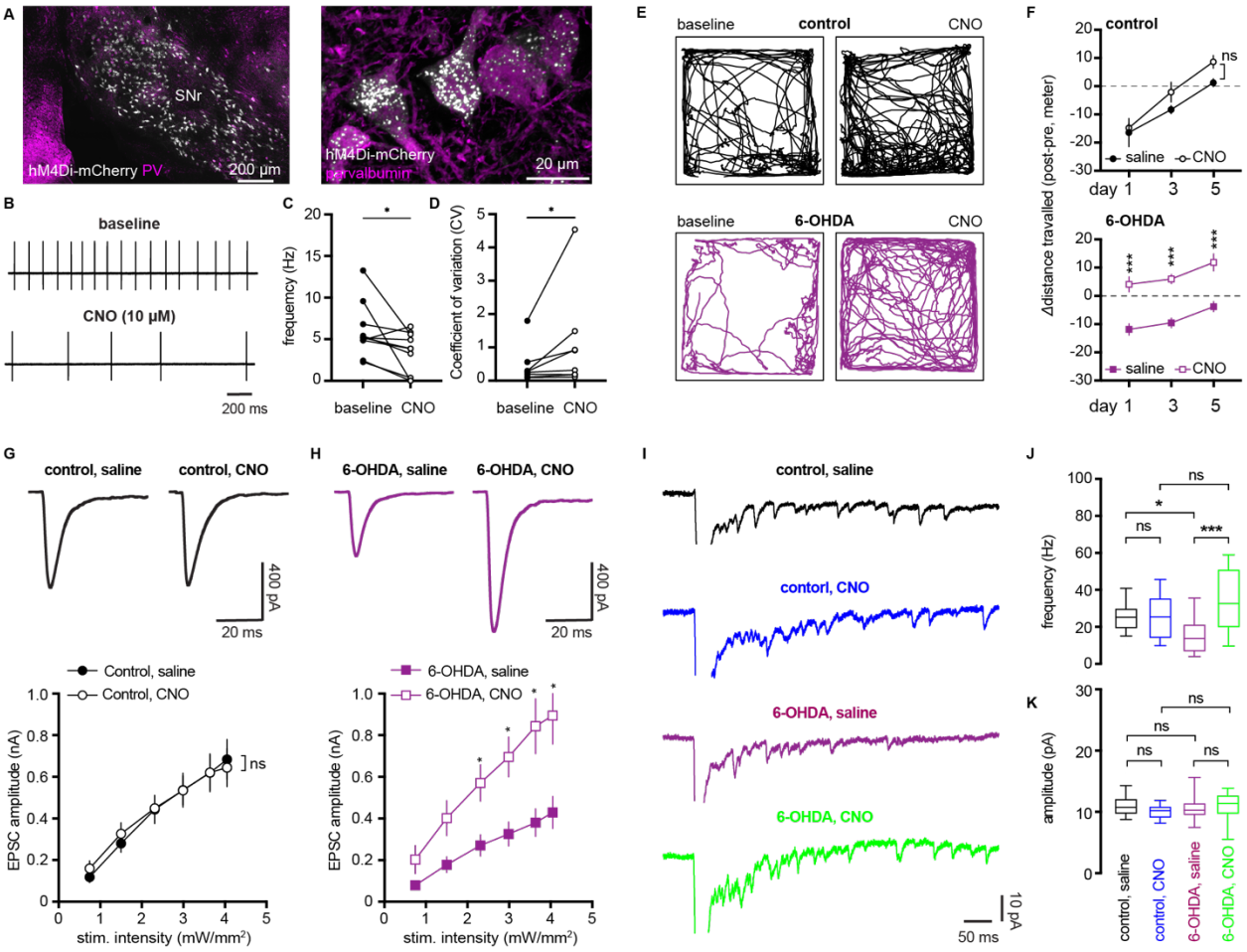

**Figure 7**. **Basal ganglia output drives the synaptic adaptations in M1 following the loss of SNc DA neurons**. **A**) Representative confocal images showing hM4Di-mcherry expression in the PV-expressing SNr neurons under low and high magnifications. Similar number of SNr neurons were infected between groups (controls = 276 [160–357] neurons/slice, n = 20 slices/10 mice; 6-OHDA = 233 [170–271] neurons/slice, n = 23 slices/12 mice; $p$ = 0.08, MWU). **B**) Representative traces of the autonomous firing of a SNr neuron from a DA-depleted mouse prior to and after CNO application. **C-D**) Box plots showing that hM4Di activation by CNO effectively suppressed the frequency (C, baseline = 5.2 [4.3–7.5] Hz, CNO = 3.9 [0.27–5.6] Hz; n = 10 neurons/3 mice; $p$ = 0.02, WSR) and regularity (D, CV of ISIs, baseline = 0.27 [0.13–0.49], CNO = 0.61 [0.19–1.35]; n = 10 neurons/3 mice; $p$ = 0.016, WSR) of the SNr neuronal firing. **E**) Representative track plots showing the effects of CNO injections to locomotor activity of controls and 6-OHDA mice in an open field on day 5. **F**) Summarized results showing the difference of distance travelled in an open field arena between pre- and post-saline/CNO injections in controls and 6-OHDA mice. Behavioral tested were conducted on days 1, 3 and 5. **G-H**) hM4Di activation did not alter the amplitude of optogenetically-evoked thalamocortical EPSCs in PT neurons from controls (G, $p$ = 0.9, mixed effects model), but increased the amplitude of optogenetically-evoked thalamocortical EPSCs in PT neurons from 6-OHDA mice (H, $p$ = 0.007, mixed effects model followed by Sidak's test). Top, representative traces of oEPSCs in PT neurons; Bottom, summarized results. 18-24 neurons from 3-4 mice for each group. **I**) Representative traces of optogenetically-evoked $Sr^{2+}$-EPSCs in controls and 6-OHDA mice treated with saline or CNO. **J**) Summarized results showing CNO injection did not alter the frequency of $Sr^{2+}$-EPSCs in slices from controls (control/saline = 25 [19–30] Hz, control/CNO = 25 [14–35] Hz; $p > 0.9$), but decreased the frequency of $Sr^{2+}$-EPSCs in slices from 6-OHDA mice (6-OHDA/saline = 13.8 [6.7–21.3] Hz, 6-OHDA/CNO = 32.4 [19.6–50.8] Hz, $p$ = 0.0001). **K**) Summarized results showing CNO injection did not alter the amplitude of $Sr^{2+}$-EPSCs in slices from either controls (control/saline = 10.7 [9.7–12.1] pA, n= 18 neurons/3 mice; control/CNO = 10.2 [9.1–10.9] pA, n = 18 neurons/3 mice; $p$ = 0.8) or 6-OHDA mice (6-OHDA/saline = 10.3 [9.5–11.4] pA, n= 22 neurons/3 mice; 6-OHDA/CNO = 11.4 [9.7–12.7] pA, n = 19 neurons/3 mice; $p$ = 0.95). Kruskal-Wallis test followed by Dunn's tests.

PV-Cre mice with SNr hM4Di expression in PV-expressing SNr neurons were subcutaneously injected with either CNO (1.0 mg/kg, at 12 hrs interval between injections) or saline for 5 consecutive days to continuously disrupt the abnormal basal ganglia outputs, or control for subcutaneous injections. Open filed locomotor activities were measured on days 1, 3 and 5. Difference in the total distance travelled prior to and post injections were comparable between CNO-injected and saline-injected control mice (**Figure 7E, F**). This is perhaps because that CNO's effects to unilateral SNr neuronal activity of DA intact mice were not sufficient to robustly affect general motor activity. In contrast, CNO injection significantly increased the locomotor activity of 6-OHDA mice relative to saline injected mice (**Figure 7E, F**). These data indicate that the SNr neurons

of 6-OHDA mice were more sensitive to hM4Di activation and that chemogenetic suppression of SNr outputs and/or disruption of pathologic oscillation was associated with immediate behavioral effects in 6-OHDA mice (*42*, *45*). These results also confirm that chemogenetic approach could effectively alter basal ganglia outputs and lead to physiological and behavioral phenotypes.

To determine whether disruption of pathological BG outputs could rescue adaptive changes of M1 circuits, the same cohort of mice described above also received retrobeads injection into the pons to retrogradely label M1 PT neurons and ChR2(H134R)-eYFP injection into the BGMT for optogenetic stimulation of thalamocortical synapses to PT neurons. In vehicle-injected control mice, we found that chemogenetic suppression of SNr activity through repetitive CNO injection did not alter the amplitude of optogenetically evoked thalamic oEPSCs in PT neurons (**Figure 7G**). In contrast, repetitive CNO injection significantly increased the amplitude of optogenetically evoked thalamic oEPSCs in PT neurons of 6-OHDA mice (**Figure 7H**).

Further, we assessed the effects of chemogenetic suppression of SNr activity to quantal properties of thalamocortical transmission to PT neurons. Chemogenetic suppression of SNr activity through repetitive CNO injection did not alter either the frequency or the amplitude of optogenetically-evoked thalamic $Sr^{2+}$-EPSCs in PT neuros of vehicle-injected control mice (**Figure 7I-K**). In contrast, repetitive CNO injection significantly increased the frequency, but not the amplitude, of optogenetically evoked thalamic $Sr^{2+}$-EPSCs in PT neurons of 6-OHDA mice (**Figure 7I-K**). Together, these data suggest that chemogenetic suppression of basal ganglia outputs could rescue the

decreased thalamocortical transmission to M1 PT neurons in 6-OHDA mice, perhaps via the disruption of synchronized bursting pattern of BG-thalamocortical activity.

Our recent study reported a decreased intrinsic excitability of M1 PT neurons in parkinsonism (*26*). To interrogate the impact of chemogenetic suppression of basal ganglia output on cellular excitability of M1 PT neurons, retrogradely labelled PT neurons were targeted for current clamp recording. In vehicle-injected control mice, continuous CNO injections for 5 days did not alter the intrinsic excitability of M1 PT neurons (**Supplementary figure 4**). In 6-OHDA mice, CNO injections for 5 days tended to increase the excitability of M1 PT neurons, but the effects did not reach statistical significance (**Supplementary figure 4**). These data suggest that adaptation of the intrinsic excitability of PT neurons perhaps involves additional mechanisms.

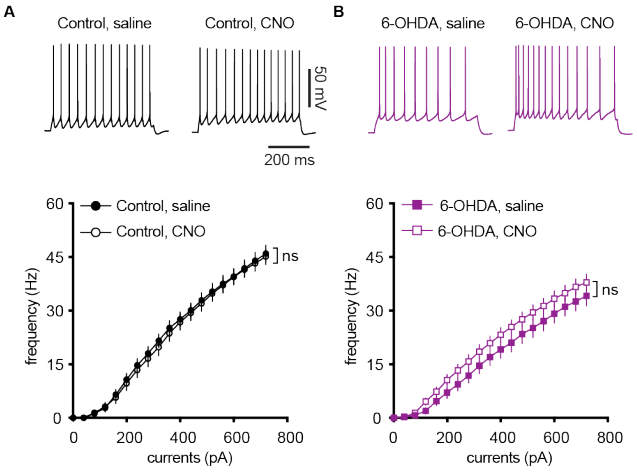


**Supplementary figure 4**. **Chemogenetic suppression of basal ganglia output does not affect intrinsic excitability of M1 PT neurons**. **A**) Representative traces of action potentials of PT neurons from saline- and CNO-injected control mice (top) and summarized results (bottom, $p$ = 0.29, two-way ANOVA,). **B**) Representative traces of action potentials of PT neurons from saline- and CNO-injected 6-OHDA mice (top) and summarized results (bottom, mixed effects model, $p$ = 0.18).

## Discussion

The present study provides novel insights into motor cortical circuitry adaptations following the degeneration of SNc DA neurons. We demonstrated that DA depletion induces cell-subtype- and input-specific downregulation of thalamic excitation to M1 PT neurons (**Figure 1**). Physiological and anatomical analyses showed that the weakened thalamocortical synaptic strength is likely associated with a loss of thalamocortical synapses (**Figure 2–4**). Moreover, NMDARs are enriched at thalamocortical synapses to M1 PT neurons (**Figure 5**). Prolonged NMDARs activation *ex vivo* was sufficient to decrease thalamocortical excitation to M1 PT neurons from control animals, but such effects were occluded in 6-OHDA mice (**Figure 6**). These data suggest that excessive NMDARs activation *in vivo* is involved in mediating the decreased thalamocortical transmission after DA depletion. In addition, chemogenetic suppression of the SNr activity can reverse the disrupted thalamocortical transmission in parkinsonian mice (**Figure 7**), suggesting that pathological pattern of BG activity perhaps drives cortical circuitry dysfunction in parkinsonian state. Last, we showed that synaptic and intrinsic adaptations of M1 PT neutrons in parkinsonism are mediated by different molecular mechanisms.

The impact of BG dysfunction on M1 outputs is expected to be more complicated than it has been proposed, considering the complexity of cortical circuit and its plasticity mechanisms. Consistently, relative to IT neurons, PT neurons are more vulnerable to DA degeneration and their activities are robustly entrained by the pathological oscillations through the transition of the motor thalamus (*12*, *16*, *21*, *26*, *27*, *37*). Although these two pyramidal neuron subtypes in the L5 of M1 differ in their gene expression, morphology, and electrophysiological properties (*46*–*48*), the excitatory inputs from the motor thalamus

to them are comparable (*10*). Thus, we posited that additional cellular and circuit mechanisms are involved and contribute to cell-subtype-selective changes in parkinsonian state. As expected, we observed a series of intrinsic (*26*) and synaptic adaptations in M1 of DA-depleted mice (**Figures 1–4**), mainly affecting PT neurons. Thus, both cellular and synaptic adaptations in M1 play a critical role in the reduced motor cortical outputs and impaired motor control in parkinsonian state (*12*, *14*, *17*, *21*, *31*, *49*, *50*). On the other hand, the weakened thalamic excitation is less likely to drive the abnormally synchronized burst firing of PT neurons in parkinsonian state (**Figure 4**). Further studies should explore the potential involvement of other circuit mechanisms, such as the intralaminar cortical connections or GABAergic network.

Discrepancies exist regarding changes in the rate of thalamic firing after DA depletion, which can be due to the methodological difference (*15*, *37*, *51*). However, reports consistently suggest robust synchronization and strong entrainment of cortical neurons by thalamic activity in parkinsonian state (*16*, *37*). Such an abnormal temporal patterning and adaptive changes in cellular excitability of thalamic neurons could evoke rebound excitation and perhaps contribute to an overall increase of firing frequency of BGMT neurons (*15*, *42*, *43*). Consistently, the weakened thalamic excitation to PT neurons can be rescued by chemogenetically disrupting BG-thalamus interaction (**Figure 7**), indicating a key role of BG pathological activity in driving M1 circuit dysfunction. This finding might be relevant to the therapeutic effects of levodopa or deep brain stimulation in PD, since both treatments could effectively suppress the pathological oscillations in the basal ganglia and alleviate motor deficits. A thorough investigation of BG control of

cortical activity in parkinsonian stage remains needed using experimental approaches with better temporal resolution.

Enhanced bursting pattern of activity is expected to be more effective in triggering glutamate release at thalamocortical axon terminals in M1 (*52*). Considering the enrichment of GluN2B-containing NMDARs receptors at the thalamic synapses to PT (**Figure 5**) (*39*, *53*), chronic activation of NMDARs of PT neurons by the excessive glutamate could be a key molecular mechanism underlying the weakened thalamocortical connection in parkinsonian state (**Figure 6**). Such mechanisms have been reported in other brain areas and under different neurological conditions (*34*, *53*–*55*), which may subsequently activate ubiquitin-proteasome pathway (*54*, *56*), or cathepsin B-like protease activity that regulates actin-based cytoskeleton to mediate morphological changes (*57*). It's worth noting that adaptive changes at the distal dendrites of the L1 were not properly assessed in current physiology studies due to the limitation of experimental approaches and thus future work is needed to explore this field using complementary approaches, such as voltage imaging technologies.

In addition to the detrimental effects of pathological BG-thalamocortical activity, impaired DA neuromodulation in M1 may play a role in cortical dysfunction in PD (*58*). However, the mesocortical DA projections mainly arise from the ventral tegmental area in rodents (*59*), which are less affected in the model of the present studies. Thus, it is unlikely that loss of DA neuromodulation in M1 plays a significant role in the observations described in the present study. However, M1 receives robust midbrain DA inputs in primates (*60*) and the impact of their degeneration on cortical function in PD should be considered and further explored.

*Conclusion*

Altogether, we demonstrated that degeneration of SNc DA neurons triggers cell-subtype- and input-specific adaptations in M1. Our studies also highlight that synaptic and intrinsic alterations in M1 are mediated by different circuitry and molecular mechanisms. While the present study focuses on thalamocortical synaptic adaptations and potential molecular mechanisms, future studies should continue to explore adaptive changes in the motor cortex and understand their roles in PD pathophysiology and treatment.

## Materials and Methods

*Animals*

Wild-type (WT) C57BL/6J mice of both sexes (3–4 month-old, RRID:IMSR_JAX:000664) were obtained from the Van Andel Research Institute vivarium internal colony and used in the study. Homozygous PV-Cre knock-in mice were originally purchased from Jackson laboratories (stock# 017320RRID: IMSR_JAX:017320, Bar Harbor, ME) and maintained at a C57/BL6J background in Van Andel Research Institute vivarium. Mouse genotyping was conducted through the service of Transnetyx, Inc (Cordova, TN). Mice were housed up to four animals per cage under a 12/12 h light/dark cycle with access to food and water *ad libitum* in accordance with NIH guidelines for care and use of animals. All animal studies were reviewed and approved by the Institutional Animal Care and Use Committee at Van Andel Research Institute (reference#: 22-02-006).

*Stereotaxic surgery for 6-OHDA and virus injections*

Mice were randomly assigned to different treatment groups. Mice were mounted and secured in a stereotaxic frame (Kopf) under 2% isoflurane anesthesia. Throughout the procedure, body temperature of the mouse was maintained by a thermostatic heating pad. Once the skull was opened, small holes were drilled above the pre-determined targets to inject: 1) 6-OHDA (3–4 µg) into the medial forebrain bundle (MFB, from bregma (in mm), anterior-posterior (AP) = -0.7, mediolateral (ML) = +1.2, and dorsoventral (DV) = -4.7 from the brain surface) to induce unilateral degeneration of nigrostriatal pathway, or vehicle into the MFB to serve as vehicle-injected controls; 2) retrobeads (200 nl, 10x dilution) into the ipsilateral pontine nuclei (from bregma (in mm), AP = -5.0, ML = +0.6, DV = -5.0) or

contralateral striatum (from bregma (in mm), AP = +0.2, ML = -2.3, DV = -2.9) to retrogradely label PT and IT neurons, respectively; and 3) AAV9-hSyn-ChR2(H134R)-eYFP (RRID:Addgene_127090, 300 nl at a titer of $3.6x10^{12}$ GC/ml) into the ventral subregion of the motor thalamus (from bregma (in mm), AP = -1.6, ML = 0.8, DV = -4.3) to label thalamocortical axon terminals for optogenetics studies. *Post hoc* histology analysis showed that the AAV infected most of the ventral medial and ventral anteriolateral (VM/VAL, Figure 1) thalamus that receives GABAergic basal ganglia outputs (referred as "BGMT"). A small cohort of mice also received pAAV9-hSyn-DIO-hM4D(Gi)-mCherry (RRID:Addgene_44362, 300 nl at a titer of $2.2x10^{12}$ GC/ml) injection into the substantia nigra pars reticulata (from bregma (in mm), AP = -3.4, ML = +1.4, DV = -4.6) for chemogenetic studies. For morphology studies, AAVrg-hSyn-eGFP (RRID:Addgene_50465, 300 nl at 2x $10^{13}$ GC/ml) were injected into the pontine nuclei to retrogradely label PT neuron in the motor cortex. All injection were performed using a 10 µl syringe (Hamilton, Reno, NV) mounted on a motorized microinjector (Stoelting, Wood Dale, IL) at a speed of 100 nl/min. Details of the stereotaxic injection procedure can be found on Protocol.io (dx.doi.org/10.17504/protocols.io.rm7vzye28lx1/v1)

*Slice preparation for electrophysiology*

3–4 weeks post-injections, brain slices were prepared for electrophysiology. Mice were anesthetized with avertin (250–300 mg/kg), followed by transcardial perfusion with ice-cold sucrose-based artificial cerebrospinal fluid (aCSF) equilibrated with 95% $O_2$/5% $CO_2$ and containing (in mM): 230 sucrose, 26 $NaHCO_3$, 10 glucose, 10 MgSO4, 2.5 KCl, 1.25 $NaH_2PO_4$, 0.5 $CaCl_2$, 1 sodium pyruvate and 0.005 L-glutathione. Coronal brain sections

(250 μm) containing the primary motor cortex were prepared using a vibratome (VT1200s, Leica, RRID:SCR_018453) in the same sucrose-based solution that was maintained at ~4 °C using a recirculating chiller (FL300, Julabo, Allentown, PA). Slices were then held in aCSF equilibrated with 95% $O_2$/5% $CO_2$ and containing (in mM): 126 NaCl, 26 $NaHCO_3$, 10 glucose, 2 $MgSO_4$, 2.5 KCl, 1.25 $NaH_2PO_4$, 1 sodium pyruvate and 0.005 L-glutathione at 35 °C for 30 min for recovery and then at room temperature until electrophysiology recordings or NMDA incubation.

*Brain slice physiology and optogenetics*

Brain slices were placed in recording chamber with continuous perfusion of recording solution containing (in mM): 126 NaCl, 26 $NaHCO_3$, 10 glucose, 3 KCl, 1.6 $CaCl_2$, 1.5 $MgSO_4$, and 1.25 $NaH_2PO_4$. The solution was equilibrated with 95% $O_2$/5%$CO_2$ and maintained at 33–34 °C using feedback controlled in-line heater (TC-324C, Warner Instruments). To assess synaptic strength, TTX (1 μM) and 4-AP (100 μM) were routinely included to isolate optogenetically evoked monosynaptic thalamocortical or corticocortical EPSCs in M1. To test the effectiveness of thalamic driving of M1 neuronal firing (Figure 4), TTX/4-AP were omitted from the recording solution and a selective $GABA_A$ receptor antagonist SR-95531 (GABAzine) was added to prevent the recruitment of GABAergic inhibitions. Neurons were visualized using a CCD camera (SciCam Pro, Scientifica, UK) and SliceScope Pro 6000 system (Scientifica, UK) integrated with a BX51 upright microscope and motorized micromanipulators. Retrogradely labelled neurons in the layer 5 were targeted under a 60x water immersion objective lens (Olympus, Japan) for whole-cell patch clamp recording using a MultiClamp 700B amplifier (RRID:SCR_018455) and

Digidata 1550B controlled by pClamp 11 software (Molecular Devices, San Jose, CA; RRID:SCR_011323). Data were sampled at 50 KHz. Borosilicate glass pipettes (O.D. = 1.5 mm, I.D. = 0.86 mm, length = 10 cm, item#: BF150-86-10, Sutter Instruments, Novato, CA) were pulled by micropipette puller (P1000, Sutter instrument, Novato, CA; RRID:SCR_021042) and used for patch clamp recording with a resistance of 3–6 MOhm when filled with (1) cesium methanesulfonate-based internal solution of (in mM): 120 $CH_3O_3SCs$, 2.8 NaCl, 10 HEPES, 0.4 $Na_4$-EGTA, 5 QX314-HBr, 5 phosphocreatine, 0.1 spermine, 4 ATP-Mg, and 0.4 GTP-Na (pH 7.3, 290 mOsm); or (2) K-gluconate based internal solution, containing (in mM): 140 K-gluconate, 3.8 NaCl, 1 $MgCl_2$, 10 HEPES, 0.1 $Na_4$-EGTA, 2 ATP-Mg, and 0.1 GTP-Na (pH 7.3, 290 mOsm). Optogenetic stimulation was delivered using a 478 nm LED (pE-300$^{Ultra}$, CoolLED, UK; RRID:SCR_021972) through a 60x objective lens (Olympus). Electrophysiology data were analyzed and quantified using Clampfit 11.1 (Molecular Devices, San Jose, CA; RRID:SCR_011323). Peak amplitude of AMPARs-mediated EPSCs at -80 mV was quantified as a measure of synaptic strength. To calculate NMDA/AMPA ratio, amplitude of NMDA-mediated currents at +40 mV was measured at 50 ms post-optogenetic stimulation when AMPARs EPSCs largely decay to baseline level.

*Immunohistochemistry*

Brain tissues after electrophysiology brain slice preparation were fixed in 4% PFA in 0.1 M phosphate buffer overnight at 4 °C and then were resected into 70–100 μm slices using a VT1000s vibratome (Leica Biosystems, Deer Park, IL; RRID:SCR_016495) to prepare brain sections for immunohistochemistry of tyrosine hydroxylase (TH). In vGluT2

stereology and neuronal morphology studies, mice were perfused with ice-cold phosphate-buffered saline (PBS, pH = 7.4) for 5 min and subsequently with 4% PFA mice for 30 min. The brain was then extracted and saved in 4% PFA overnight at 4 °C before being resected into 70 μm slices using a VT1000s vibratome (Leica Biosystems, Deer Park, IL; RRID:SCR_016495) for immunohistochemistry or morphology studies.

Brain slices were rinsed 3x with PBS before being incubated with 0.2% Triton X-100 and 2% normal donkey serum (Sigma-Aldrich) for 60 min at room temperature. Brain slices were then incubated with primary antibodies, including mouse anti-TH (1:2000, cat# MAB318, Sigma-Aldrich; RRID:AB_2201528), or guinea pig anti-vGluT2 (cat# 135404, Synaptic Systems, RRID:AB_887884) for 48 hours at 4 °C or overnight at room temperature. Sections were then rinsed 3x with PBS and incubated with secondary antibodies for 90 min, including donkey anti-mouse Alexa Fluor 488 (Cat# 715-545-150; Jackson ImmunoResearch Labs, West Grove, PA; RRID:AB_2340846), donkey anti-mouse Alexa Fluor 594 (Cat# 715-585-150; Jackson ImmunoResearch Labs, West Grove, PA; RRID:AB_2340854), or donkey anti-guinea pig Alexa Fluor 488 (Cat# 706-545-148; Jackson ImmunoResearch Labs, West Grove, PA; RRID:AB_2340472), at room temperature before washing with PBS for 3 times. Brain sections were mounted with VECTASHIELD antifade mounting medium (Cat# H-1000, Vector Laboratories, Newark, CA; RRID:AB_2336789), were cover-slipped and sealed with nail polish. TH- and vGluT2-immunoreactivity (ir) was imaged under 20x or 40x objective lens using an Olympus DP80 camera through an Olympus BX63F microscope, or a confocal laser scanning microscope (A1R, Nikon, Japan; RRID:SCR_020317). TH-ir of control and 6-OHDA mice was quantified by normalizing the striatal TH-ir from the ipsilateral side to the value from the

contralateral hemisphere, with a subtraction of background measured from the cerebral cortex.

*Animal behavior*

To assess parkinsonian motor deficits, mice were subject to 1) open field locomotion test, where their locomotor activity and rotations were monitored for 10 min and quantified using Anymaze software (Stoelting, Wood Dale, IL); (2) cylinder test using a 600-ml glass beaker to assess the spontaneous forelimbs use during weight-bearing touches which were recorded using a digital camcorder at 60 fps (Panasonic, HC-V180K) and analyzed off-line by a researcher blinded to treatments. 3 weeks post-surgery, vehicle- or 6-OHDA-injected mice received subcutaneous saline- or water-soluble clozapine-n-oxide (CNO, 1 mg/kg body weight, cat# HB6149, HelloBio, Princeton, NJ) injections for chemogenetic studies. The injections were conducted at 7 am and 7 pm each day for 5 consecutive days. Locomotion tests (10 min) were performed 30 min after subcutaneous injections on days 1, 3 and 5 to measure the behavioral effects. Following behavioral tests, animals were used to prepare brain slices for physiology studies. All physiology recordings were started ~3 hours post saline or CNO injections.

*Confocal imaging and digital image analysis*

vGluT2-ir was collected from the layers 5A and 5B under a 100x objective using a Nikon A1R confocal microscope. Z stack Images with a 0.15 μm interval were taken under the identical settings, including laser power, gain, pinhole size, and scanning speed etc. between animals. The density of vGluT2-ir was estimated based on the immunostaining signals between 5 and 8 μm below the surface of slices using the optical dissector method (*61*). For spine density analysis and

dendritic examination, segments of basal dendrites were tracked down from the cell bodies of retrogradely labeled PT neurons in M1 and imaged under an oil-immersion 100x objective using the confocal microscope (NA = 1.45; x/y, 1024 X 1024 pixels; z step = 0.5 μm, A1R, Nikon). The distance from the soma to the basal dendrites analyzed was 50–100 μm. eGFP-labeled segments of the apical dendrites were selected from the layer I. To quantify spine density and dendritic diameter, only microscopic image data with ample eGFP expression and high signal-to-noise ratios were included. Spine density analysis was performed using Imaris software (version 9.3, Oxford, UK; RRID:SCR_007370). Briefly, 2-3 dendritic segments from the layer I and the layer V measuring 20–30 microns in length were reconstructed three-dimensionally using Imaris' filament tracer function from each confocal image. Spines were then manually traced, reconstructed, and quantified. For accurate three-dimensionally reconstruction, both the dendrite segments and spines were recomputed automatically based on the manual traces. To quantify dendritic diameter, dendritic segments (30–40 μm in length) were traced and straightened using ImageJ (NIH, Bethesda, MD; RRID:SCR_003070). A grid (grid type: lines with 2 μm intervals; area per point: 5 $\mu m^2$; center grid on image) was placed over top of the dendritic segments and cross-sectional measurements were taken along the dendrite at each grid mark (control: 240 and 262 measurements from 3 mice for the layer I and V, respectively; 6-OHDA: 240 and 267 measurements from 3 mice for the layer I and V, respectively).

*Statistics*

Statistics analysis was performed in GraphPad Prism 9 (GraphPad Software, San Diego, CA; RRID:SCR_002798). Nonparametric Mann-Whitney U (MWU) test, Wilcox signed rank (WSR) test, and Kruskal–Wallis test followed by Dunn's Multiple Comparisons (as indicated in the text) were used to compare the medians of 2 or 3 groups in order to minimize the assumption of dataset normality. For experiments with nested design

wherein more than one cells were sampled from each animal, a mixed effects model was used to compare group difference where the responses (e.g., EPSCs amplitude, AP frequency, etc.) were modeled as a combination of a fixed effect (i.e., vehicle versus 6-OHDA injections; or saline versus CNO injections) and random effects associated with each animal. Behavioral results in the Figure 7 were analyzed using repeated measures two-way ANOVA. Whenever applicable, *post hoc* Šídák's multiple comparisons test was performed. Data were collected from 3-8 mice per study. Individual animals were considered independent samples. All statistic tests were two tailed with $p$ values < 0.05 (*), 0.01 (**), or 0.001 (***) as thresholds for statistical significance. Data are reported as median plus interquartile ranges.

**Data availability.** The datasets generated during and/or analyzed during the current study are available from the corresponding author on reasonable request.

## References cited


1. R. L. Albin, A. B. Young, J. B. Penney, The functional anatomy of basal ganglia disorders. *Trends Neurosci*. 12, 366–375 (1989).

2. A. Galvan, T. Wichmann, Pathophysiology of parkinsonism. *Clin Neurophysiology Official J Int Fed Clin Neurophysiology*. 119, 1459–74 (2008).

3. M. M. McGregor, A. B. Nelson, Circuit mechanisms of Parkinson's disease. *Neuron*. 101, 1042–1056 (2019).

4. K. C. Nakamura, A. Sharott, P. J. Magill, Temporal Coupling with Cortex Distinguishes Spontaneous Neuronal Activities in Identified Basal Ganglia-Recipient and Cerebellar-Recipient Zones of the Motor Thalamus. *Cereb Cortex*. 24, 81–97 (2014).

5. E. Kuramoto, T. Furuta, K. C. Nakamura, T. Unzai, H. Hioki, T. Kaneko, Two Types of Thalamocortical Projections from the Motor Thalamic Nuclei of the Rat: A Single Neuron-Tracing Study Using Viral Vectors. *Cereb Cortex*. 19, 2065–2077 (2009).

6. C. Bosch-Bouju, B. I. Hyland, L. C. Parr-Brownlie, Motor thalamus integration of cortical, cerebellar and basal ganglia information: implications for normal and parkinsonian conditions. *Front Comput Neurosc*. 7, 163 (2013).

7. Á. L. Bodor, K. Giber, Z. Rovó, I. Ulbert, L. Acsády, Structural correlates of efficient GABAergic transmission in the basal ganglia–thalamus pathway. *J Neurosci*. 28, 3090–3102 (2008).

8. C. J. Lobb, A. K. Zaheer, Y. Smith, D. Jaeger, In vivo electrophysiology of nigral and thalamic neurons in alpha-synuclein-overexpressing mice highlights differences from toxin-based models of parkinsonism. *J Neurophysiol*. 110, 2792–2805 (2013).

9. B. J. Hunnicutt, B. R. Long, D. Kusefoglu, K. J. Gertz, H. Zhong, T. Mao, A comprehensive thalamocortical projection map at the mesoscopic level. *Nat Neurosci*. 17, 1276–1285 (2014).

10. B. M. Hooks, T. Mao, D. A. Gutnisky, N. Yamawaki, K. Svoboda, G. M. G. Shepherd, Organization of Cortical and Thalamic Input to Pyramidal Neurons in Mouse Motor Cortex. *J Neurosci*. 33, 748–760 (2013).

11. M. Gaidica, A. Hurst, C. Cyr, D. K. Leventhal, Distinct Populations of Motor Thalamic Neurons Encode Action Initiation, Action Selection, and Movement Vigor. *J Neurosci*. 38, 6563–6573 (2018).

12. F. Aeed, N. Cermak, J. Schiller, Y. Schiller, Intrinsic Disruption of the M1 Cortical Network in a Mouse Model of Parkinson's Disease. *Movement Disord*. 36, 1565–1577 (2021).

13. B. I. Hyland, S. Seeger-Armbruster, R. A. Smither, L. C. Parr-Brownlie, Altered recruitment of motor cortex neuronal activity during the grasping phase of skilled reaching in a chronic rat model of unilateral Parkinsonism. *J Neurosci*. 39, 0720–19 (2019).

14. B. Pasquereau, M. R. DeLong, R. S. Turner, Primary motor cortex of the parkinsonian monkey: altered encoding of active movement. *Brain*. 139, 127–143 (2016).

15. C. Bosch-Bouju, R. A. Smither, B. I. Hyland, L. C. Parr-Brownlie, Reduced Reach-Related Modulation of Motor Thalamus Neural Activity in a Rat Model of Parkinson's Disease. *J Neurosci*. 34, 15836–15850 (2014).

16. E. Brazhnik, A. J. McCoy, N. Novikov, C. E. Hatch, J. R. Walters, Ventral Medial Thalamic Nucleus Promotes Synchronization of Increased High Beta Oscillatory Activity in the Basal Ganglia–Thalamocortical Network of the Hemiparkinsonian Rat. *J Neurosci*. 36, 4196–4208 (2016).

17. B. A. Sauerbrei, J.-Z. Guo, J. D. Cohen, M. Mischiati, W. Guo, M. Kabra, N. Verma, B. Mensh, K. Branson, A. W. Hantman, Cortical pattern generation during dexterous movement is input-driven. *Nature*. 577, 386–391 (2020).

18. K. V. Shenoy, M. Sahani, M. M. Churchland, Cortical Control of Arm Movements: A Dynamical Systems Perspective. *Annu Rev Neurosci.* 36, 337–359 (2012).

19. A. P. Georgopoulos, A. F. Carpenter, Coding of movements in the motor cortex. *Curr Opin Neurobiol*. 33, 34–39 (2015).

20. M. R. DeLong, Primate models of movement disorders of basal ganglia origin. *Trends Neurosci*. 13, 281–285 (1990).

21. B. Pasquereau, R. S. Turner, Primary motor cortex of the parkinsonian monkey: differential effects on the spontaneous activity of pyramidal tract-type neurons. *Cereb Cortex*. 21, 1362–1378 (2011).

22. J. A. Goldberg, T. Boraud, S. Maraton, S. N. Haber, E. Vaadia, H. Bergman, Enhanced Synchrony among Primary Motor Cortex Neurons in the 1-Methyl-4-Phenyl-1,2,3,6-Tetrahydropyridine Primate Model of Parkinson's Disease. *J Neurosci*. 22, 4639–4653 (2002).

23. L. Guo, H. Xiong, J.-I. Kim, Y.-W. Wu, R. R. Lalchandani, Y. Cui, Y. Shu, T. Xu, J. B. Ding, Dynamic rewiring of neural circuits in the motor cortex in mouse models of Parkinson's disease. *Nat Neurosci*. 18, 1299–1309 (2015).

24. R. M. Villalba, J. A. Behnke, J.-F. Pare, Y. Smith, Comparative Ultrastructural Analysis of Thalamocortical Innervation of the Primary Motor Cortex and Supplementary Motor Area in Control and MPTP-Treated Parkinsonian Monkeys. *Cereb Cortex* (2021), doi:10.1093/cercor/bhab020.

25. J. Cousineau, L. Lescouzères, A. Taupignon, L. Delgado-Zabalza, E. Valjent, J. Baufreton, M. L. Bon-Jégo, *Eneuro*, in press, doi:10.1523/eneuro.0081-20.2020.

26. L. Chen, S. Daniels, Y. Kim, H.-Y. Chu, Cell Type-Specific Decrease of the Intrinsic Excitability of Motor Cortical Pyramidal Neurons in Parkinsonism. *J Neurosci*. 41, 5553–5565 (2021).

27. O. K. Swanson, R. Semaan, A. Maffei, *Eneuro*, in press, doi:10.1523/eneuro.0548-19.2021.

28. A. R. Brown, B. Hu, M. C. Antle, G. C. Teskey, Neocortical movement representations are reduced and reorganized following bilateral intrastriatal 6-hydroxydopamine infusion and dopamine type-2 receptor antagonism. *Exp Neurol*. 220, 162–170 (2009).

29. R. Viaro, M. Morari, G. Franchi, Progressive motor cortex functional reorganization following 6-hydroxydopamine lesioning in rats. *J Neurosci*. 31, 4544–4554 (2011).

30. E. K. Plowman, N. J. Thomas, J. A. Kleim, Striatal Dopamine Depletion Induces Forelimb Motor Impairments and Disrupts Forelimb Movement Representations within the Motor Cortex. *J Park Dis*. 1, 93–100 (2011).

31. J. S. Biane, Y. Takashima, M. Scanziani, J. M. Conner, M. H. Tuszynski, Thalamocortical Projections onto Behaviorally Relevant Neurons Exhibit Plasticity during Adult Motor Learning. *Neuron*. 89, 1173–1179 (2016).

32. L. Petreanu, D. Huber, A. Sobczyk, K. Svoboda, Channelrhodopsin-2–assisted circuit mapping of long-range callosal projections. *Nat Neurosci*. 10, 663–668 (2007).

33. G. Turrigiano, Too Many Cooks? Intrinsic and Synaptic Homeostatic Mechanisms in Cortical Circuit Refinement. *Annu Rev Neurosci*. 34, 89–103 (2011).

34. H.-Y. Chu, E. L. McIver, R. F. Kovaleski, J. F. Atherton, M. D. Bevan, Loss of hyperdirect pathway cortico-subthalamic inputs following degeneration of midbrain dopamine neurons. *Neuron*. 95, 1306-1318.e5 (2017).

35. J. Ding, J. D. Peterson, D. J. Surmeier, Corticostriatal and Thalamostriatal Synapses Have Distinctive Properties. *J Neurosci*. 28, 6483–6492 (2008).

36. A. Oswal, P. Brown, V. Litvak, Synchronized neural oscillations and the pathophysiology of Parkinson's disease. *Curr Opin Neurol*. 26, 662–670 (2013).

37. K. C. Nakamura, A. Sharott, T. Tanaka, P. J. Magill, Input Zone-Selective Dysrhythmia in Motor Thalamus after Dopamine Depletion. *J Neurosci*. 41, 10382–10404 (2021).

38. O. H. Miller, A. Bruns, I. B. Ammar, T. Mueggler, B. J. Hall, Synaptic Regulation of a Thalamocortical Circuit Controls Depression-Related Behavior. *Cell Reports*. 20, 1867–1880 (2017).

39. M. Lafourcade, M.-S. H. van der Goes, D. Vardalaki, N. J. Brown, J. Voigts, D. H. Yun, M. E. Kim, T. Ku, M. T. Harnett, Differential dendritic integration of long-range inputs in association cortex via subcellular changes in synaptic AMPA-to-NMDA receptor ratio. *Neuron* (2022), doi:10.1016/j.neuron.2022.01.025.

40. H. Wang, G. G. Stradtman, X.-J. Wang, W.-J. Gao, A specialized NMDA receptor function in layer 5 recurrent microcircuitry of the adult rat prefrontal cortex. *Proc National Acad Sci*. 105, 16791–16796 (2008).

41. E. L. McIver, J. F. Atherton, H.-Y. Chu, K. E. Cosgrove, J. Kondapalli, D. Wokosin, D. J. Surmeier, M. D. Bevan, Maladaptive downregulation of autonomous subthalamic nucleus activity following the loss of midbrain dopamine neurons. *Cell Reports*. 28, 992-1002.e4 (2019).

42. J. Kim, Y. Kim, R. Nakajima, A. Shin, M. Jeong, A. H. Park, Y. Jeong, S. Jo, S. Yang, H. Park, S.-H. Cho, K.-H. Cho, I. Shim, J. H. Chung, S.-B. Paik, G. J. Augustine, D. Kim, Inhibitory Basal Ganglia Inputs Induce Excitatory Motor Signals in the Thalamus. *Neuron*. 95, 1181-1196.e8 (2017).

43. E. K. Bichler, F. Cavarretta, D. Jaeger, *Eneuro*, in press, doi:10.1523/eneuro.0436-20.2021.

44. E. Brazhnik, A. V. Cruz, I. Avila, M. I. Wahba, N. Novikov, N. M. Ilieva, A. J. McCoy, C. Gerber, Judith. R. Walters, State-Dependent Spike and Local Field Synchronization between Motor Cortex and Substantia Nigra in Hemiparkinsonian Rats. *J Neurosci*. 32, 7869–7880 (2012).

45. S. Seeger-Armbruster, C. Bosch-Bouju, S. T. C. Little, R. A. Smither, S. M. Hughes, B. I. Hyland, L. C. Parr-Brownlie, Patterned, But Not Tonic, Optogenetic Stimulation in Motor Thalamus Improves Reaching in Acute Drug-Induced Parkinsonian Rats. *J Neurosci*. 35, 1211–1216 (2015).

46. B. A. Suter, M. Migliore, G. M. G. Shepherd, Intrinsic electrophysiology of mouse corticospinal neurons: a class-specific triad of spike-related properties. *Cereb Cortex*. 23, 1965–1977 (2013).

47. G. M. G. Shepherd, Corticostriatal connectivity and its role in disease. *Nat Rev Neurosci*. 14, 278–291 (2013).

48. H. Peng, P. Xie, L. Liu, X. Kuang, Y. Wang, L. Qu, H. Gong, S. Jiang, A. Li, Z. Ruan, L. Ding, Z. Yao, C. Chen, M. Chen, T. L. Daigle, R. Dalley, Z. Ding, Y. Duan, A. Feiner, P. He, C. Hill, K. E. Hirokawa, G. Hong, L. Huang, S. Kebede, H.-C. Kuo, R. Larsen, P. Lesnar, L. Li, Q. Li, X. Li, Y. Li, Y. Li, A. Liu, D. Lu, S. Mok, L. Ng, T. N. Nguyen, Q. Ouyang, J. Pan, E. Shen, Y. Song, S. M. Sunkin, B. Tasic, M. B. Veldman, W. Wakeman, W. Wan, P. Wang, Q. Wang, T. Wang, Y. Wang, F. Xiong, W. Xiong, W. Xu, M. Ye, L. Yin, Y. Yu, J. Yuan, J. Yuan, Z. Yun, S. Zeng, S. Zhang, S. Zhao, Z. Zhao, Z. Zhou, Z. J. Huang, L. Esposito, M. J. Hawrylycz, S. A. Sorensen, X. W. Yang, Y. Zheng, Z. Gu, W. Xie, C. Koch, Q. Luo, J. A. Harris, Y. Wang, H. Zeng, Morphological diversity of single neurons in molecularly defined cell types. *Nature*. 598, 174–181 (2021).

49. L. Wang, J. M. Conner, J. Rickert, M. H. Tuszynski, Structural plasticity within highly specific neuronal populations identifies a unique parcellation of motor learning in the adult brain. *Proc National Acad Sci*. 108, 2545–2550 (2011).

50. R. Hasegawa, T. Ebina, Y. R. Tanaka, K. Kobayashi, M. Matsuzaki, Structural dynamics and stability of corticocortical and thalamocortical axon terminals during motor learning. *Plos One*. 15, e0234930 (2020).

51. M. Pessiglione, D. Guehl, A.-S. Rolland, C. François, E. C. Hirsch, J. Féger, L. Tremblay, Thalamic Neuronal Activity in Dopamine-Depleted Primates: Evidence for a Loss of Functional Segregation within Basal Ganglia Circuits. *J Neurosci*. 25, 1523–1531 (2005).

52. J. R. Eles, K. C. Stieger, T. D. Y. Kozai, The temporal pattern of intracortical microstimulation pulses elicits distinct temporal and spatial recruitment of cortical neuropil and neurons. *J Neural Eng*. 18, 015001 (2021).

53. O. H. Miller, A. Bruns, I. B. Ammar, T. Mueggler, B. J. Hall, Synaptic Regulation of a Thalamocortical Circuit Controls Depression-Related Behavior. *Cell Reports*. 20, 1867–1880 (2017).

54. R. Meller, S. J. Thompson, T. A. Lusardi, A. N. Ordonez, M. D. Ashley, V. Jessick, W. Wang, D. J. Torrey, D. C. Henshall, P. R. Gafken, J. A. Saugstad, Z.-G. Xiong, R. P. Simon, Ubiquitin Proteasome-Mediated Synaptic Reorganization: A Novel Mechanism Underlying Rapid Ischemic Tolerance. *J Neurosci*. 28, 50–59 (2008).

55. M. J. Hasbani, M. L. Schlief, D. A. Fisher, M. P. Goldberg, Dendritic Spines Lost during Glutamate Receptor Activation Reemerge at Original Sites of Synaptic Contact. *J Neurosci*. 21, 2393–2403 (2001).

56. H. J. Kim, J. J. Waataja, S. A. Thayer, Cannabinoids Inhibit Network-Driven Synapse Loss between Hippocampal Neurons in Culture. *J Pharmacol Exp Ther*. 325, 850–858 (2008).

57. S. Graber, S. Maiti, S. Halpain, Cathepsin B-like proteolysis and MARCKS degradation in sub-lethal NMDA-induced collapse of dendritic spines. *Neuropharmacology*. 47, 706–713 (2004).

58. J. Cousineau, V. Plateau, J. Baufreton, M. L. Bon-Jégo, Dopaminergic modulation of primary motor cortex: From cellular and synaptic mechanisms underlying motor learning to cognitive symptoms in Parkinson's disease. *Neurobiol Dis*. 167, 105674 (2022).

59. J. A. Hosp, H. E. Nolan, A. R. Luft, Topography and collateralization of dopaminergic projections to primary motor cortex in rats. *Exp Brain Res*. 233, 1365–1375 (2015).

60. B. Berger, P. Gaspar, C. Verney, Dopaminergic innervation of the cerebral cortex: unexpected differences between rodents and primates. *Trends Neurosci*. 14, 21–27 (1991).

61. M. J. West, Stereological methods for estimating the total number of neurons and synapses: issues of precision and bias. *Trends Neurosci*. 22, 51–61 (1999).